A distinctive Eocene Asian monsoon and modern biodiversity resulted from the rise of eastern Tibet

Journal Item

How to cite:

He, Songlin; Ding, Lin; Xiong, Zhongyu; Spicer, Robert A.; Farnsworth, Alex; Valdes, Paul J.; Wang, Chao; Cai, Fulong; Wang, Houqi; Sun, Yong; Zeng, Deng; Xie, Jing; Yue, Yahui; Zhao, Chenyuan; Song, Peiping and Wu, Chen (2022). A distinctive Eocene Asian monsoon and modern biodiversity resulted from the rise of eastern Tibet. Science Bulletin (Early access).

Link(s) to article on publisher's website:
http://dx.doi.org/doi:10.1016/j.scib.2022.10.006

Article

A distinctive Eocene Asian monsoon and modern biodiversity resulted from the rise of eastern Tibet

Songlin He, Lin Ding, Zhongyu Xiong, Robert A. Spicer, Alex Farnsworth, Paul J. Valdes, Chao Wang, Fulong Cai, Houqi Wang, Yong Sun, Deng Zeng, Jing Xie, Yahui Yue, Chenyuan Zhao, Peiping Song, Chen Wu

PII: S2095-9273(22)00453-4
DOI: https://doi.org/10.1016/j.scib.2022.10.006
Reference: SCIB 1898

To appear in: *Science Bulletin*

Received Date: 1 June 2022
Revised Date: 16 September 2022
Accepted Date: 16 September 2022

Please cite this article as: S. He, L. Ding, Z. Xiong, R.A. Spicer, A. Farnsworth, P.J. Valdes, C. Wang, F. Cai, H. Wang, Y. Sun, D. Zeng, J. Xie, Y. Yue, C. Zhao, P. Song, C. Wu, A distinctive Eocene Asian monsoon and modern biodiversity resulted from the rise of eastern Tibet, *Science Bulletin* (2022), doi: https://doi.org/10.1016/j.scib.2022.10.006

Article

A distinctive Eocene Asian monsoon and modern biodiversity resulted from the rise of eastern Tibet

Songlin He [a,b], Lin Ding [a,b,*], Zhongyu Xiong [a], Robert A. Spicer [a,c,d], Alex Farnsworth [a,e], Paul J. Valdes [e], Chao Wang [a,b], Fulong Cai [a,b], Houqi Wang [a], Yong Sun [a], Deng Zeng [a,b], Jing Xie [a], Yahui Yue [a], Chenyuan Zhao [a,b], Peiping Song [a], Chen Wu [a]

[a] *State Key Laboratory of Tibetan Plateau Earth System, Environment and Resources (TPESER), Institute of Tibetan Plateau Research, Chinese Academy of Sciences, Beijing 100101, China*

[b] *University of Chinese Academy of Sciences, Beijing 100049, China*

[c] *Key Laboratory of Tropical Forest Ecology, Xishuangbanna Tropical Botanical Garden, Chinese Academy of Sciences, Mengla 666303, China*

[d] *School of Environment, Earth and Ecosystem Sciences, the Open University, Milton Keynes MK7 6AA, UK*

[e] *School of Geographical Sciences, University of Bristol, Bristol BS8 1SS, UK*

*** Corresponding author.**

E-mail address: dinglin@itpcas.ac.cn (L. Ding)

Recevied 2022-06-01，revised 2022-09-16，accepted 2022-09-16

Abstract:

The uplift of eastern Tibet, Asian monsoon development and the evolution of globally significant Asian biodiversity are all linked, but in obscure ways. Sedimentology, geochronology, clumped isotope thermometry, and fossil leaf-derived numerical climate data from the Relu Basin, eastern Tibet, show at ~50–45 Ma the basin was a hot (mean annual air temperature, MAAT, ~27 °C) dry desert at low-elevation of 0.6 ± 0.6 km. Rapid basin rise to 2.0 ± 0.9 km at 45–42 Ma and to 2.9 ± 0.9 km at 42–40 Ma, with MAATs of ~20 and ~16 °C, respectively, accompanied seasonally varying increased annual precipitation to >1500 mm. From ~39 to 34 Ma, the basin attained 3.5 ± 1.0 km, near its present-day elevation (~3.7 km), and MAAT cooled to ~6 °C. Numerically-modelled Asian monsoon strength increased significantly when this Eocene uplift of eastern Tibet was incorporated. The simulation/proxy congruence points to a distinctive Eocene Asian monsoon, quite unlike that seen today, in that it featured bimodal precipitation and a winter-wet regime, and this enhanced biodiversity modernisation across eastern Asia. The Paleogene biodiversity of Asia evolved under a continually modifying monsoon influence, with the modern Asian monsoon system being unique to the present and a product of a long gradual development in the context of an ever-changing Earth system.

Keywords: Paleoelevation, Asian monsoon, Biodiversity, Fossil, Eastern Tibet, Relu Basin

1. Introduction

Himalayan-Tibetan Plateau orography influences the Asian monsoon system and global climate by acting as a high-altitude heat source and deflecting air-flow [1–6]. Moreover, the growth of this vast topographic feature and its effects on climate, have been primary determinants in the diversification and evolution of the globally exceptional regional biota [7–11]. Today, eastern Tibet serves as the link and gateway between the high and generally semi-arid plateau interior and the extraordinarily rich biota of southeast Asia, while itself hosting unique and highly diverse Hengduan Mountain ecosystems [7,8,12]. Quantifying how and when eastern Tibet developed its modern high and topographically complex form is critical to understanding its influences on climatic and biotic evolution, and in particular the Asian monsoon system.

Today's Asian monsoon system is complex, but is broadly divisible into the South Asian monsoon (SAM) and the East Asian monsoon (EAM), as well as a transition area (TA) across eastern Tibet and Yunnan where they interact [13]. Collectively, the SAM, EAM and TA display a pronounced seasonal precipitation cycle with relatively dry winters and wet summers [1,13]. This is especially so for the SAM, which dominates precipitation over India, southern Tibet and parts of Indo-China, and although SAM initiation has been generally attributed to the development of the Himalayan-Tibetan highland, mechanisms underlying its evolution are extensively debated [4,5,14–17]. Modelling and proxy work has pointed to the existence of a strong monsoon system over southern Asia since at least the Eocene [18–22], but this Eocene monsoon remains poorly characterized [15,19,20] and the relationship between the rise of eastern Tibet and modern monsoon development remains unknown.

Sedimentological and paleobotanical evidence indicate that prior to the expansion and amplification of the Asian monsoonal climate, eastern Tibet in the early Paleogene was an arid region [23–25] dominated by a sub-tropical high-pressure system [26,27]. Large-scale aeolian sediments or "red beds" occur at the bottom of Paleogene basins from eastern Tibet to the interior of the Sichuan

Basin [23,24,28] suggesting a widespread hot-dry climate. By the late Eocene-early Oligocene, the presence of fossils of subtropical broadleaved plants in the Markam, Jianchuan, Lühe and Wenshan basins [12,29–32], as well as the existence of lacustrine and swampy facies [28], indicate that eastern Tibet, extending into Yunnan, had undergone an arid-to-humid transition possibly in response to monsoon expansion linked to orogeny [24,28]. However, temporally continuous sedimentological records are lacking for any single basin. Furthermore, whether such an expanded Eocene Asian monsoon is consistent with the form and characteristics of the modern monsoon needs to be assessed. The initiation of monsoons on deep-geological timescales does not necessarily imply they were identical, or even similar to, modern monsoon systems [16].

The Hengduan Mountains that form much of eastern Tibet host one of Earth's most important biodiversity hotspots [7,8]. Recently, radiometric re-dating of abundant Paleogene floras in this region [12,29] have provided insights into regional evolutionary history and, more broadly, Asian biodiversity origins. The question now arises as to whether there are other unknown paleontological records that could be combined with well-dated continuous sedimentological successions to further explore complex links between Tibetan Plateau orogeny, climate and the biota.

The Relu Basin in eastern Tibet (Fig. 1a and Fig. S1 online), tectonically located in the southern part of the Yidun terrane and geographically in the hinterland of the Hengduan Mountains, covers an area of ~220 km^2 (Fig. 1b) and encompasses an elevation range of 3400–4200 m. The basin contains continuous arid-to-humid sedimentological records, diverse plant and animal fossils, and multiple layers of datable volcanic rocks, and is a key area for decoding the relationship between the Cenozoic uplift history of eastern Tibet, the evolution of the Asian monsoon and biodiversity. Nevertheless, detailed studies of the Relu Basin are limited, with previous studies only focused on provenance analysis and tectonic nature of the basin [33,34]. Here, based on a well-constrained absolute dating framework spanning ~50–34 Ma, we reconstruct quantitatively the uplift history of the Relu Basin using clumped and oxygen isotopes of paleosol nodules, together with ancient moist enthalpy signatures decoded from leaf fossils. By quantifying paleoclimatic conditions through numerical analysis of leaf form and model simulations, we show that a monsoonal system, distinct from the modern in that it featured bimodal precipitation with particularly humid winters, took root in the Relu Basin after 45 Ma, synchronous with the uplift of eastern Tibet. We also emphasize that the rise of eastern Tibet, and the initiation of an amplified and expanded Eocene monsoon, greatly enhanced environmental niche heterogeneity, transforming a previously desert region into the globally significant biodiversity center that it is today.

Fig. 1. Geological map of the Relu Basin. (a) Modern major tectonic terranes and features of the Tibetan Plateau and modern dominant airflow showing the location of the study area (red star). The Asian climate system today encompasses the East Asian monsoon (EAM, cyan shaded area), the South Asian monsoon (SAM, blue shaded area), a transitional area (TA, yellow shaded area) where they overlap, and westerlies. The modern Asian monsoon areas are as recognised by Wang and Ho [13]. Abbreviations: RL, Relu Basin; NQ, Nangqian Basin; GJ, Gonjo Basin; MK, Markam Basin; JC, Jianchuan Basin; LJ, Lijiang Basin; SP, Songpan Basin; LP, Lunpola Basin; LMS, Longmen Shan; AKMS, Ayimaqin-Kunlun-Mutztagh suture zone; JS, Jinsha suture zone; GLS, Ganzi-Litang suture zone; BNS, Bangong-Nujiang suture zone; IYS, Indus-Yalong suture zone. (b) Detailed geological map of the Relu Basin, showing the Changzong Formation (E_2c) and the Relu Formation (E_2r) together with the locations of measured sections with analysed samples. (c) Geological cross-section A–A′ showing the main structures and strata in the Relu Basin, and the locations of the fossil-bearing and volcanic tuff layers. (d) Generalized lithologic column of the Relu Basin strata with corresponding lithology, age constraint and representative fossils.

2. Methods

2.1. Zircon U-Pb geochronology

For volcanic tuff and sandstone samples, the U-Pb dating of selected zircons was conducted by using an Agilent 7500a ICP-MS coupled with a New Wave UP 193FX laser ablation system installed at the State Key Laboratory of Tibetan Plateau Earth System, Environment and Resources (TPESER), Institute of Tibetan Plateau Research, Chinese Academy of Sciences (ITPCAS). Analytical details are described in the Supplementary materials (online), and all data are reported in Table S1 (online).

2.2. Plant fossil Preparation, photography and CLAMP analysis

The 2429 plant fossil specimens used in this study are curated in terms of their individual layers at TPESER, ITPCAS, and were photographed digitally under artificial light with Canon R5 camera and micro-lens. We divided the leaf fossils into morphotypes based on their architecture, and identified well-preserved specimens to generic or family level. To decode the paleoclimate and paleoelevation signal preserved in the TR1 and TR3 fossil assemblages, Climate-Leaf Analysis Multivariate Program (CLAMP) was calibrated using the modern PhysgAsia2 physiognomic file paired with 1-km resolution gridded climate dataset, WorldClim2 [35]. Numerical description and scoring of leaf physiognomic characteristics followed the CLAMP protocols (http://clamp.ibcas.ac.cn). The score sheets and CLAMP results are available as Tables S2–S4 (online).

2.3. Paleosol nodule sampling and identification

Carbonate nodule samples were collected from 54 layers of paleosols in the Changzong Formation and 43 layers of paleosols in the upper Relu Formation within five measured sections (Fig. S2 online). From each layer of paleosols we collected at least 20 nodules with no apparent diagenesis as determined in the field using a handheld magnifier. All nodules were collected from a depth of 40 cm below the paleosol surface horizons to minimize possible evaporative effects or post-depositional alteration [36]. All samples used for isotope analyses were examined under a stereomicroscope to select samples with fresh micritic surfaces without penetrating calcite veins. Then the selected samples were made into thin sections for mineral analysis and visual diagenesis assessment using a Zeiss Axio Imager.M2m optics microscope at TPESER, ITPCAS and CL8200 MK5-2 cathodoluminescence microscopy at the Chengdu University of Technology (CDUT). The main mineral types and corresponding contents of the paleosol nodules were further determined through X-ray diffraction (XRD) analysis by using a Philips X'pert PRO MRD system at CDUT.

2.4. Oxygen and carbon isotope measurement

C-O analyses of paleosol, limestone clasts, and mammal tooth samples were performed on a MAT 253 gas source mass spectrometer coupled with GasBench II at the Laboratory for Stable Isotope Geochemistry, Institute of Geology and Geophysics, Chinese Academy of Sciences. Powder samples were obtained using a low-speed microdrill from fresh surfaces under a binocular stereoscope to avoid overheating and potential C-O redistribution. Analytical details and raw data are provided in the Supplementary materials (online).

2.5. Carbonate clumped isotope analysis

We performed pedogenic carbonate clumped isotope analyses at TPESER, ITPCAS. Each powder sample (~8 mg) was digested using 1 mL anhydrous phosphoric acid in a common acid bath at 90 °C for 15 min. After acid digestion, the generated CO_2 samples were then purified off-line and eventually entered into a MAT 253plus gas source mass spectrometer to obtain the raw Δ_{47} data. Laboratory methods are detailed in the Supplementary materials (online). Carbonate formation temperatures ($T(\Delta_{47})$) were converted using the thermometer of Kelson et al. [37]. All raw data related to the clumped and stable isotopes are provided in Tables S5–S9 (online).

2.6. Climate model simulations

We used an updated fully-coupled atmosphere-ocean general circulation model (HadCM3BL-M2.1aD) with a spatial resolution of 2.5° × 3.75° latitude by longitude with 19 vertical levels in the atmosphere and 20 vertical levels in the ocean. Sea-ice was calculated on a zero-layer model. Vegetation was predicted as a fraction for each grid-box using a dynamical vegetation model TRIFFID and the land surface scheme MOSES 2.1. HadCM3BL-M2.1aD has shown skill in reproducing both modern, Quaternary, and deep-time climates compared to observations, as well as for monsoons and Tibetan climate [2].

A fully equilibrated (10,422 years) Lutetian (~47 Ma) and Bartonian (~37 Ma) simulation set at 1120-ppm pCO_2 were used for the basis of three topographic sensitivity studies for Tibet. (1) Bartonian topography where Tibetan topography (22.5°–40°N, 70°–105°E) was flattened (0 m). (2) Lutetian dual mountain and valley (4.5-km Gangdese, 4-km Central Watershed mountains and 1.5-km Central Valley) system. (3) Bartonian dual mountain and valley system, with the eastern end raised to 3.5 km. Each sensitivity experiment was run for 500 years (means calculate from the last 100 years). Detailed methods are available in the Supplementary materials (online).

3. Results

3.1. Stratigraphy and dating framework in the Relu Basin

3.1.1. Stratigraphy

Cenozoic strata in the Relu Basin form a monoclinal structure that dips towards the northeast (Fig. 1c) and are divided from bottom to top into two stratigraphic units (Fig. 1d): the Changzong Formation and the overlying Relu Formation, having a combined thickness of ~2 km. The lithology and ages of the two units are constrained through the measurement of five stratigraphic sections (Relu, Sewen, Naxi, Quzha, and Ningyoite; Fig. S2 online) and U-Pb dating of volcanic rocks within the basin. The lithologies are summarized below and detailed in the Supplementary materials (online).

The Changzong Formation (E_2c) is a purplish red, planar, siliciclastic succession that is ~450–

960 m thick (Fig. S3a online) and unconformably overlies Triassic flysch and a granite pluton. The formation consists mainly of alternating purplish red conglomerates, coarse to medium-grained sandstones, siltstones, paleosols (Fig. S3b online), and intercalated pyroclastic rocks (Fig. S3c online). The conglomerate and mudstone successions are typical alluvial fan deposits, while some of the sandstones are well-sorted and exhibit large-scale high-angle (~30°) planar cross-bedding interpreted as aeolian dune facies. Grain size analysis and the surface morphology of quartz grains (Fig. S4 and Table S10 online) further indicate these sandstones are aeolian in origin, and are comparable with aeolian dunes preserved in the basal units of the neighboring Gonjo and Jianchuan basins [23,24,28]. Overall, the Changzong Formation preserves a series of alluvial fan–aeolian dune facies deposits formed in an arid environment.

The Relu Formation (E_2r) is divided into lower and upper members (E_2r^1 and E_2r^2; Fig. S3d online). The lower Relu Formation is ~370–950 m thick and comprises interbedded varicolored mudstone and shale (Fig. S3e online), intercalated with fine sandstone, siltstone, limestone, marl, and volcanic tuffs and exhibits lacustrine sedimentary structures, including ripple marks, rain marks and varved sediments, which we interpret as representing lacustrine deposition. Fossil aquatic organisms such as ostracods, gastropods, and charophytes were found in the limestone, marls and shale, further suggesting that this member is lacustrine in origin and represents sedimentation under relatively humid conditions. Three distinct plant-fossil assemblages (TR1 to TR3 in ascending order) occur in this member at the Relu section (Fig. S3f–h online), and evidence an extremely diverse species composition.

The upper Relu Formation, ~380–500 m thick (Fig. S3k online), consists mainly of purplish red sandstone, lenticular conglomerate, and multiple layers of interbedded mudstones and paleosols (Fig. S3l online). The lithologies and small-scale cross-bedding suggest the upper Relu Formation comprises fluvial facies sediments that formed when the paleo-lakes were shrinking, reflecting shallower sedimentation water depths compared to the lower Relu Formation, but still generally representing a relatively humid climatic background. Vertebrate, especially mammalian, fossils of diverse species (mainly *Anthracokeryx Litangensis*, *Caenolophus proficiens*, *Sianodon* sp., *Bothriodon* sp., and *Yuomys* sp.) have been collected from the upper Relu Formation, also indicate humid conditions.

3.1.2. Dating framework

The weighted mean age of the youngest zircon cluster with an *n* value of ≥3 (YC2σ(3+)) constrains well the maximum deposition age (MDA) of the strata [38]. Sandstones from the lowest of the Changzong Formation at the Sewen and Naxi sections (samples 2018TR81 and 2018TR215), yield YC2σ(3+) ages of 50.1 ± 0.8 Ma (*n* = 10, MSWD = 1.3; Fig. S5a online) and 49.6 ± 0.9 Ma (*n* = 8, MSWD = 1.0; Fig. S5b online), respectively. Therefore, the maximum depositional age of the Changzong Formation is ~50 Ma. Zircon U-Pb analyses of two pyroclastic layers near the lower (sample 2018TR86) and upper (samples 2018TR84 and 2019TR159; Fig. S3c online) part of the Changzong Formation in the Relu section yield Concordia ages of 48.0 ± 0.2 Ma (2σ, *n* = 58; Fig. 2a) and 45.2/45.3 ± 0.1 Ma (2σ, *n* = 57/194; Fig. 2b, c), respectively. The pyroclastic rocks (sample 2020TR48) immediately overlying the aeolian dunes of the Changzong Formation in the Sewen section in the southern part of the basin have an age of 45.3 ± 0.1 Ma (2σ, *n* = 62; Fig. 2d), which dates the cessation of aeolian deposition. Pyroclastic rocks (sample 2018TR83) from the upper part of the Changzong Formation in the northern basin yield the same age of 45.2 ± 0.2 Ma (2σ, *n* = 40; Fig. 2e). Therefore, this upper layer of volcanic material (45 Ma) defines the youngest age of this unit, and the depositional age range of the Changzong Formation is constrained to ~50–45 Ma.

A volcanic tuff layer (sample 2020TR56; Fig. S3i online) in the Relu Section located between the TR2 and TR3 fossil-bearing layers has a Concordia age of 42.0 ± 0.1 Ma (2σ, *n* = 170; Fig. 2f), while another volcanic tuff layer above the TR3 fossil-bearing layer (samples 2019TR210 and 2020TR09; Fig. S3j online) has Concordia ages of 40.1 ± 0.1 (2σ, *n* = 100; Fig. 2h) and 40.3 ± 0.1

Ma (2σ, $n = 172$; Fig. 2i). In addition, the volcanic tuff layer (sample 2020TR58) in the lower part of the lacustrine strata in the Sewen section also yields a Concordia age of 42.00 ± 0.1 Ma (2σ, $n = 115$; Fig. 2g), suggesting that it marks the same stratigraphic horizon as the 42 Ma volcanic tuff in the Relu section. Therefore, based on the ages of the two volcanic tuff layers in the lower Relu Formation, and the underlying pyroclastic rocks (45 Ma; Fig. S3c online) in the upper part of Changzong Formation, the lacustrine sequence of the lower Relu Formation spans ~45 to 40 Ma with the TR1 and TR2 fossil-bearing layers being 45–42 Ma and the TR3 layer being 42–40 Ma.

The mammalian fossils of the upper Relu Formation also indicate the depositional age. Species such as *Yuomys* sp., of the Ctenodactyloidea, existed no later than the late Eocene in China [39] and serve as index fossils constraining the upper Relu Formation to the latest Eocene (~34 Ma). Moreover, the youngest zircons from sandstones from the lowest part of the upper Relu Formation at the Quzha and Ningyoite sections (samples 2019TR54 and 2019TR15) yield the maximum deposition ages of 38.8 ± 0.6 Ma (YC2σ(3+), $n = 5$, MSWD = 0.2; Fig. S5c online) and 39.3 ± 0.4 Ma (YC2σ(3+), $n = 5$, MSWD = 0.3; Fig. S5d online), respectively, constraining the upper Relu Formation to range from ~39 to 34 Ma.

Fig. 2. Concordia zircon U–Pb ages and weighted-mean plots for volcanic rocks in the Relu Basin. (a) Pyroclastic rocks from the lower part of the Changzong Formation (E_2c) in the Relu section. (b), (c) Pyroclastic rocks from the upper part of the Changzong Formation (E_2c) in the Relu section. (d) Pyroclastic rocks from the upper part of the Changzong Formation (E_2c) in the Sewen section. (e) Pyroclastic rocks from the upper part of the Changzong Formation (E_2c) in the Naxi section. (f) Tuff from the lower part of the lower Relu Formation (E_2r^1) in the Relu Section. (g) Tuff from the lower part of the lower Relu Formation (E_2r^1) in the Sewen section. (h), (i) Tuffs from the middle part of the lower Relu Formation (E_2r^1) in the Relu section. The error bars and ellipses represent 2σ.

3.2. Plant fossil assemblages

Plant fossils, including leaves and rare fruits (Fig. 3a–z), are well preserved in argillaceous siltstones of the lower Relu Formation lacustrine strata at the Relu section, and occur in three distinct layers designated as assemblages TR1 to TR3 numbered from bottom to top. A total of 775 specimens so far collected form the TR1 assemblage (Fig. S6 online) include over 25 morphotypes of woody dicots meeting the minimum diversity requirement (*n* = 20) of the CLAMP. This assemblage includes mainly "*Eucalyptus*" sp. (alternatively attributable to "*Myrtophyllum*" [40]), *Palibinia* sp., *Dryandra sp*., *Comptonia*., *Viburnum* sp., *Hemiptelea* sp., and Fabaceae. TR2 is located above TR1 and has yielded 331 plant specimens (Fig. S7 online). In TR2 there are fewer morphotypes compared to TR1, and CLAMP analysis is limited. Heat- and drought-tolerant species such as *Palibinia* and *Dryandra* disappear, leaf size is much larger, and "*Eucalyptus*" is the main representative plant species. The TR3 plant assemblage (Fig. S8 online), above TR2, currently comprises 1323 plant specimens, including at least 40 morphotypes of woody dicot leaves, so fully satisfying the CLAMP minimum diversity requirement ($n \geq 20$ morphotypes/species). In addition to "*Eucalyptus*" sp., this assemblage also includes *Pistacia* sp., *Ulmus* sp., *Toxicodendron* sp., *Lonicera* sp., *Myrica* sp., *Syzygium* sp., *Rhus* sp., *Alstonia* sp., *Evodia* sp., *Zelkova* sp., *Ficus* sp., *Populus sp*., and *Hemiptelea* sp., etc. The species richness increases markedly from TR1 to TR3, but "*Eucalyptus*" remains most abundant.

Most of the leaf fossils are small, thick, have a leathery texture, and generally possess an entire (untoothed) leaf margin, although sometimes teeth are present (Fig. 3a–z). Leaf trait (CLAMP) analysis indicates a warm and seasonally wet/dry environment as detailed below. Based on assemblage composition, the vegetation represents a subtropical evergreen broad-leaved forest dominated by "*Eucalyptus*" sp., with a limited number of evergreen, deciduous, broad-leaved, and thermophilic small trees or shrubs in the understory, or at the forest margins.

Fig. 3. Representative Eocene fossil taxa in the Relu Basin. All scale bars in plant fossils are 1 cm. (a), (o) "*Eucalyptus*" (Myrtaceae) leaves. (b) *Pistacia* leaf. (c) *Ulmus* leaf. (d) *Toxicodendron* leaf. (e) *Drimycarpus* leaf. (f) *Ficus* leaf. (g) *Populus* leaf. (h) *Lonicera* leaf. (i) Apocynaceae leaflet. (j) *Marsilea* leaf. (k) *Zelkova ungeri* Kovats leaf. (l) Apiaceae leaflet. (m) cf. *Thunbergia* leaf. (n) Uknown fruits. (p1) cf. *Dryandra* leaf. (p2) cf. *Comptonia* leaf. (p3) *Palibinia* leaf. (q)

Elaeagnus leaf. (r) Anacardiaceae leaf. (s) *Myrica* leaf. (t) Apocynaceae leaf. (u) *Hemiptelea paradavidii* leaf. (v) Fabaceae leaf. (w) Fagaceae leaf. (x) *Cotula* leaf. (y) *Chamaecyparis* leaf. (z) Unknown spined fruit. TR1 assemblage: (p), (v), and (w); TR2 assemblage: (n) and (o); TR3 assemblage: (a)–(m), (q)–(u), and (x)–(z). See Figs. S6–S8 (online) for more details on TR1 through TR3 assemblages. (aa) and (bb) Fossil rhinocerotid teeth.

3.3. Proxy-derived paleoclimate

Environmental reconstruction using the CLAMP (http://clamp.ibcas.ac.cn) allows us to quantify both the paleoclimate and paleoelevation of the Relu Basin during 45–40 Ma, as the morphotypes of the TR1 and TR3 fossil assemblages fully meet the CLAMP diversity requirements (all the estimated paleoclimate parameters returned by CLAMP are given in Table S3 online). Analysis of the TR1 assemblage revealed a MAAT of 20.1 ± 2.3 °C, with a mean temperature of 29.0 ± 2.9 °C in the warm month and 9.7 ± 3.5 °C in the cold month, and so indicates strong temperature seasonality. The growing season lasted nearly 12 months during which the rainfall exceeded 1500 mm with obvious seasonal variations in which the precipitation during the three consecutive wettest months (3WET) was 643 mm, while precipitation in the three consecutive driest months (3DRY) was only 92 mm (3WET:3DRY = 7:1). The composition of the TR3 assemblage suggests a relatively cooler climate than during deposition of TR1. The CLAMP-derived MAAT corresponding to TR3 was 16.2 ± 2.3 °C (~4 °C lower than TR1), with the cold-month mean temperature decreasing to 4.9 ± 3.5 °C, but a warm month mean temperature still as high as 27.6 ± 2.9 °C. The difference between the dry and wet seasons was still marked, with a 3WET/3DRY ratio of 6:1. The seasonal differences in precipitation and temperature indicate that both TR1 and TR3 record a monsoonal climate, with mean annual precipitation similar to, or even greater than, that of today (Table S3 online).

Both the vapor pressure deficits (VPDs) and the mean potential evapotranspiration (PE) recorded by TR1 and TR3 indicate much lower evaporation (higher humidity) in the winter (Table S3 online), which is the opposite of what might be expected under a SAM airflow where winters and springs are typically dry. Like most precipitation proxies CLAMP cannot determine when in the year the wet or dry seasons occurred, so for that we look to numerical climate modelling with realistic boundary conditions, including best estimates of local topography. Modern VPD measurements under SAM conditions tend to show the highest (driest) values in the spring with no clear pattern as to when the the lowest VPD occurs, while for the modern EAM and TA the lowest VPDs (most humid conditions) are almost always experienced in the winter, with no clear pattern as to when the driest conditions occur (Table S4 online).

Carbonate clumped isotopic composition (Δ_{47}) refers to the temperature dependent abundance of ^{13}C–^{18}O bonds in carbonate [41] by which carbonate formation temperature ($T(\Delta_{47})$) can be constrained [42], and this can be used to derive the paleo-surface air temperature if the isotopic composition has not been reset. Diagenesis screening indicates that the analysed paleosol nodule samples are primary in nature (refer to Supplementary text online, Fig. 4a, b, and Fig. S9 online for resetting evaluation). The Δ_{47} average value of six paleosol nodules from the Changzong Formation is 0.663‰ ± 0.010‰ (1σ; Fig. 4a and Table S5 online), and eight paleosol nodules from the upper Relu Formation have a Δ_{47} average value of 0.703‰ ± 0.010‰ (1σ; Fig. 4a and Table S5 online). To convert the Δ_{47} values into carbonate formation temperatures ($T(\Delta_{47})$), the calibration equation of Kelson et al. [37] was adopted because of its similar sample type and large temperature coverage. This gave an average $T(\Delta_{47})$ value of 33.9 ± 2.5 °C (1σ) for the Changzong Formation and 20.9 ± 3.1 °C (1σ) for the upper Relu Formation (Fig. 4a and Table S5 online). The MAAT of the Relu basin during 50–45 Ma was 27.4 ± 4.2 °C (1σ) using the empirical relationship between $T(\Delta_{47})$ and MAAT proposed by Quade et al. [44], while between 39–34 Ma, the MAAT in the basin decreased to 5.7 ± 5.2 °C (1σ; Table S5 online).

Fig. 4. Clumped, stable isotope results and predicted paleoelevations of the Relu Basin. (a) $T(\Delta_{47})$ values of representative paleosol nodules from the Changzong Formation (E_2c) and the upper Relu Formation (E_2r^2). The $T(\Delta_{47})$ values decreases 13 °C from the Changzong Formation (E_2c) to the upper Relu Formation (E_2r^2). Clumped isotope results are listed in Table S5 (online). (b) Cross-plot of the $\delta^{13}C$ and $\delta^{18}O$ values of carbonate samples. Paleosol nodule samples

from the Changzong Formation (E_2c) and the upper Relu Formation (E_2r^2) show clear differences between $\delta^{18}O_c$ values, and all these nodules exhibit very different carbon and oxygen isotopic compositions from the Triassic reworked limestone clasts. C-O isotope results are listed in Table S6 (online). (c) Paleoelevation reconstructions using the clumped and oxygen isotopes for the paleosol nodules, based on an Eocene thermodynamic fractionation model for the eastern Tibet [43]. The enlarged inverted triangles indicate average values. The $\delta^{18}O_{cw}$ values derived from the upper Relu Formation (E_2r^2) nodules produced an average elevation of 3.5+0.9/−1.0 km from ~39 to 34 Ma, while the $\delta^{18}O_{cw}$ values derived from the Changzong Formation (E_2c) nodules yield an average elevation of only 0.6 ± 0.6 km between ~50 and 45 Ma. All the paleoelevation calculation results are listed in Table S7 (online). (d) Paleoelevation reconstructions for TR1 and TR3 assemblages based on CLAMP analysis. Moist enthalpy regression using PhysgAsia2 and WorldClim2 training sets [35] with the positions of the TR1 and TR3 assemblages and MESL value derived from a climate modelling calibrated by proxy results. The moist enthalpy difference (20.10 and 28.14 kJ/kg) between sea level and the TR1 and TR3 fossil assemblages divided by the gravity constant (9.81 cm/s^2) produces elevational differences of 2.0 ± 0.9 km (45–42 Ma) and 2.9 ± 0.9 km (42–40 Ma), respectively. Error bars are 1σ.

3.4. Paleoelevation reconstruction

The paleoelevation history of the Relu Basin from ~50 to 34 Ma is derived from clumped and oxygen isotopes within paleosol nodules from the Changzong (~50−45 Ma) and upper Relu (~39−34 Ma) formations, as well as moist enthalpy derived from CLAMP of plant fossil assemblages (TR1 and TR3) in the lower Relu Formation (45−40 Ma).

3.4.1. Oxygen isotope paleoelevation estimation

Oxygen isotope paleoaltimetry is based on the empirical/theoretical decrease of meteoric water $\delta^{18}O$ values with increasing elevation [45], and if paleosol carbonate preserves faithfully the oxygen information of paleosurface water it makes it a potential paleoelevation proxy. XRD results show that the carbonate type of our analysed nodules from the Changzong and the upper Relu formations are all low-magnesium calcite (Fig. S10 online), and diagenesis screening indicates the oxygen isotopic compositions of these carbonates appear primary in nature (Supplementary text online, Fig. 4a, b, and Fig. S9 online). The $\delta^{18}O_c$ (VPDB) values of 54 paleosol nodules from the Changzong Formation yield an average value of −10.5‰ ± 0.3‰ (1σ; Fig. 4b and Table S6 online), and the calculated average $\delta^{18}O_w$ (VSMOW) value of paleosurface water is –6.4‰ ± 0.6‰ (1σ; Table S7 online) using a fractionation equation [46] combined with the $T(\Delta_{47})$ value. The average $\delta^{18}O_c$ (VPDB) values of 43 paleosol nodules from the upper Relu Formation is −12.9‰ ± 0.6‰ (1σ; Fig. 4b and Table S6 online), and return an average $\delta^{18}O_w$ (VSMOW) value of −11.4‰ ± 1.0‰ (1σ; Table S7 online).

The isotopic composition at the start of an air parcel ascent needs be known before paleoelevation can be determined via stable isotope paleoaltimetry. As global climate cooled after the Eocene [47], the $\delta^{18}O$ value for paleo-oceanic surface water at middle and low latitudes was ~1‰ lower than at present [47,48]. Recent paleomagnetic work in the Nangqian Basin [49], adjacent to the Relu Basin, showed a 3° latitude northward shift since the Eocene. Additionally, paleomagnetic research in the nearby Qiangtang terrane also showed that its late Cretaceous–Paleogene paleolatitude [50,51] was 3°–5° lower than today. Given these observations, we conservatively adopt 26°N as the Eocene paleolatitude of the Relu Basin.

Being 3° south of its present latitude (29°N) exerts an enrichment of 0.3‰ on the paleosurface water [52], so the original paleosurface water $\delta^{18}O_w$ (VSMOW) value was calculated incorporating the +0.7‰ value of paleo-oceanic water (+1‰) and paleolatitude (−0.3‰) effects. The mean value ($\delta^{18}O_{cw} = \delta^{18}O_w + 0.7‰$) of the paleosurface water $\delta^{18}O_{cw}$ (VSMOW) was adopted for the paleoelevation calculation based on an Eocene Rayleigh fractionation model (Eq. (1); [43]) deemed suitable for the eastern Tibet:

$$H = -12.4(\delta^{18}\mathrm{O_{cw}})^2 - 804.3\delta^{18}\mathrm{O_{cw}} - 3637 \ \ (R^2 = 0.79). \qquad (1)$$

The calibrated mean $\delta^{18}O_{cw}$ value of the Changzong Formation is −5.7‰ ± 0.6‰ and the calculated elevation is 570+562/−568 m, while that for the upper Relu Formation is −10.7‰ ± 1.0‰

and translates to an elevation of 3540+1008/−1020 m (Fig. 4c and Table S7 online). The uncertainties are the propagated uncertainties, which combine variations in $\delta^{18}O_c$, $T(\Delta_{47})$ values and uncertainty of the least squares regression [43] used for calculation. The apparent differences in $\delta^{18}O_{cw}$ values and calculated elevations between the Changzong Formation and the upper Relu Formation suggest that the Relu Basin floor rose from 0.6 to 3.5 km between ~50−45 and ~39−34 Ma (Fig. 5).

3.4.2. Moist enthalpy paleoelevation estimation

Moist enthalpy (H) is related to both temperature and moisture in a parcel of air and is archived well in leaf form [53]. Because moist static energy (a combination of H and potential energy) is conserved as an air parcel rises, H decreases as potential (gravitational) energy increases [54]; thus, the difference in H at two locations ($\Delta H = H_{\text{sea level}} - H_{\text{fossil site}}$), divided by the acceleration due to gravity (g, a constant with the value of 9.81 m/s^2), gives the elevation difference (Z) between those locations (Eq. (2); [54]):

$$Z = \frac{H_{\text{sea level}} - H_{\text{fossil site}}}{g}. \qquad (2)$$

CLAMP analysis reveals that the moist enthalpy of the TR1 assemblage was 321.55 ± 8.4 kJ/kg, while that of the TR3 assemblage was 313.51 ± 8.4 kJ/kg (Table S3 online). Eq. (2), shows we also need the regional H at sea level (MESL), as would be experienced by contemporaneous coastal vegetation. Since there is no coeval sea-level fossil site adjacent to the Relu Basin, we use a model-derived MESL value (337.46 kJ/kg at the paleolocation of 26°N, 100°E) for the Lutetian (Fig. S12 online) to approximate the fossil MESL. However, because model and proxy data are rarely directly comparable they are adjusted using systematic differences in model/CLAMP H values in archived coeval sea level floras at different paleolatitudes [55]. The calibrated MESL adjustment for paleolatitude is 4.19 kJ/kg using the regression equation of Su et al. [55], and this resulted in a paleolatitude-calibrated MESL value of 341.65 kJ/kg (Table S3 online). Using these values, the calculated paleoelevations for TR1 and TR3 were 2.0 ± 0.9 and 2.9 ± 0.9 km, respectively (Fig. 4d and Table S3 online). The uncertainty ($1\sigma = \pm 0.9$ km) refers to the sum of CLAMP regression uncertainties and that of the model/proxy adjustment. This indicates that the paleoelevation of the Relu Basin increased from 2.0 km (45−42 Ma) to 2.9 km (42−40 Ma) (Fig. 5).

Fig. 5. Plot of time versus elevation and climate results for eastern Tibet based on CLAMP analyses and isotope data. Error bars for individual elevation are 1σ. The red curve represents the uplift history of the eastern Tibet by using the paleoelevation results in this study. Other paleoelevation results are from the Gonjo [24], Markam [12], and Nangqian [56] basins, as well as the Longmen Shan range [57]. The locations of these basins are shown in Fig. 1a. The changes of MAAT, GSP, and 3WET/3DRY over time in the Relu Basin are represented by purple, light blue, and dark blue curves, respectively. The MAAT represented by the yellow square is based on the $T(\Delta_{47})$ values and obtained through the regression equation proposed from Quade et al. [44]. The present-day data are from the Daocheng meteorological station (29.03°N, 100.18°E; 3727.7 m a.s.l.). 3WET/3DRY, precipitation ratio between the three wettest and three driest consecutive months; GSP, growing season precipitation; MAAT, mean annual air temperature.

3.5. Numerically-modelled paleoclimate

To explore the development and form of the monsoon, we used the updated fully-coupled atmosphere-ocean general circulation model (HadCM3BL-M2.1aD) under Tibetan region topographic scenarios for the Lutetian (~47 Ma) and the Bartonian (~37 Ma), as well as a hypothetical flat Tibet scenario (Fig. S11 online).

In the Lutetian scenario (Fig. 6a1–e1), high Gangdese and Central Watershed mountains sandwich a deep-wide valley (Central Valley) with a low (open) eastern end. Our modelling shows eastern Tibet to be arid throughout the most of the year. The exception is the summer (June-July-August, JJA), but even then precipitation was less than 0.5 mm/d (Fig. 6d1). The mean annual precipitation (MAP) in the Relu Basin during the Lutetian is modelled to have been 216 mm/a (Fig. 6a1), well below the typical upper limit for defining a desert (≤250 mm/a). This arid climate is corroborated by the alluvial fan–aeolian dune deposits (desert facies) at the base of the Relu Basin, features widely distributed across eastern Tibet at this time.

In the Bartonian scenario (Fig. 6a2–e2), high topography closes the eastern end of the Central Valley and this high eastern Tibet region then becomes more humid overall (Fig. 6a3–e3), with the MAP in the Relu Basin (936 mm/a) (Fig. 6a2) exceeding that of the present-day (651 mm/a) but with a distinct bimodal seasonality. Spring (March-April-May, MAM) and autumn (September-October-November, SON) were the dominant wet seasons, both reaching 4.9 mm/d (Fig. 6c2, e2). This is very close to the 5.1 mm/d average wet season precipitation recorded today at the Daocheng meteorological station, and only slightly lower than the wet season precipitation (7.1 mm/d) recorded by Relu fossil flora. We attribute the change from arid to humid conditions seen in both proxies and modelling to the development of an Eocene Asian monsoon influence in eastern Tibet, although the seasonal form of this monsoon is quite unlike that of the present-day SAM, EAM or TA. Our modelling further indicates that, with an elevated eastern Tibet, precipitation increased across eastern Asia as a whole (Fig. 6a2), consistent with a regional development of forest ecosystems by the start of the Neogene [58]. The MAATs of the two scenarios are ~32 and ~12 °C (Fig. S12 online), observed at the location of the Relu Basin, respectively. This difference of 20 °C is close to the temperature change of 27.4 ± 4.2 to 5.7 ± 5.2 °C derived from clumped isotopes before and after the basin uplift. The relatively small difference between the models and proxy data are likely a result of (1) local topographic factors that are not resolved at the model resolution and/or (2) smaller differences in $p\mathrm{CO}_2$ and orbital configurations used in the model experiments than those expressed in the proxy data.

For the hypothetical flat Tibet scenario (Fig. 6a0–e0), with no elevated topography in the Tibetan region, most of China experiences an arid climate except for coastal areas, and the wind patterns are very zonal (west to east) throughout the year. Although not reflecting past reality, such drought induction by a low-flat model Tibet is consistent with previous sedimentary and paleobotanical studies suggesting that a wide arid/semiarid zone extended E–W across China controlled by planetary wind systems in the early Paleogene [25,58]. Our modelling shows it was the establishment of the pronounced high-landform of the eastern Tibet in the late Eocene that brought increased precipitation both to eastern Tibet and across East Asia as a whole, which then stimulated late Eocene regional biodiversification.

Fig. 6. Seasonal precipitation patterns under three different Tibetan topographic conditions. (a0)–(e0) Precipitation results for Tibetan topography flattened and set to 0 m. (a1)–(e1) Precipitation results for the Lutetian (~47 Ma) paleotopographic scenario, the Central Watershed Mountain to the north, Gangdese Mountain to the south bounding a Central Valley at 1500 m elevation. (a2)–(e2) Precipitation results for the Bartonian (~37 Ma) with a paleotopographic scenario as for the Lutetian, but with a high eastern end of the Central Valley set at 3500 m. (a3)–(e3) Precipitation results for the Bartonian minus Lutetian. (a) Annual (mm/d). (b) Boreal winter (December-January-February, DJF) (mm/d). (c) Boreal spring (March-April-May, MAM) (mm/d). (d) Boreal summer (June-July-August, JJA) (mm/d). (e) Boreal Autumn (September-October-November, SON) (mm/d). The red boxes indicate the eastern Tibet region (Lutetian: 32.5°–37.5°N, 90°–100°E; Bartonian: 27.5°–32.5°N, 98°–108°E), and the black dashed lines indicate the extent of the Gangdese, Central Watershed mountains and eastern Tibet, these regions move as model paleogeography changes over time.

4. Discussion

4.1. The rise of eastern Tibet

Our paleoelevation results show that the Relu Basin rose rapidly from a low elevation of 0.6 km at ~50–45 Ma to a moderate elevation of 2.0 km at 45–42 Ma, then to a moderate–high elevation of 2.9 km at 42–40 Ma. A further rise to 3.5 km by the late Eocene (~39 to 34 Ma) brought it close to its present-day average elevation (~3.7 km). Combined with published paleoelevation results for the Nangqian, Gonjo and Markam basins from north to south, and the Songpan Basin in the Longmen Shan range [12,24,56,57], our results constrain the Cenozoic surface uplift history across eastern Tibet (Fig. 5). Eastern Tibet remained lowland over a north–south distance of ~1000 km until the early Eocene, and then underwent a southward progressive rise so that all the surviving basins had reached or approached their present-day elevations by ~34 Ma, forming the high-landform of eastern Tibet.

Recent low-temperature thermochronological studies of eastern Tibet revealed that rapid rock exhumation occurred between 60–40 Ma for the Weixi and Deqin transects [59], and between 40–35 Ma for the Markam Basin and Lincang granite belt [60,61], all of which were interpreted as uplift effects from tectonic extrusion and upper crustal shortening, and provide further direct geological support our reconstruction of the rise of eastern Tibet. Furthermore, our paleoelevation reconstruction indicated that eastern Tibet experienced a rapid uplift during the Eocene, synchronous with crustal shortening [33] and alkaline lava eruption [62]. These events are attributed to intracontinental subduction of the Songpan-Ganzi terrane along the Jinsha suture zone [63,64]. Alternatively, or in addition, the rapid rise might be a manifestation of delamination or dripping of underlying dense mantle lithosphere in the Eocene [65].

4.2. An Eocene Asian monsoon in eastern Tibet

The sediments preserved in the Relu Basin record a transition from arid to humid conditions and the latitudinal expansion of a monsoonal climate within eastern Tibet during the Eocene. The “red beds” of the Changzong Formation at the bottom of the Relu Basin preserve alluvial fan–aeolian dune deposits that represent a particularly hot and dry climatic background. The clumped isotope-derived MAAT was 27.4 °C (Fig. 5 and Table S5 online), while climate simulations show extreme dry conditions and modelled MAAT even reaching ~32 °C (Fig. S12 online). Plants are not preserved, and may have been sparse in such hot dry conditions, so CLAMP data are unavailable. Our large-scale field surveys and previous studies [23,24,28] show similar aeolian desert deposits are present at the bottom of almost all of the Paleogene basins from eastern Tibet to the interior of the Sichuan Basin (Fig. S1 online), and likely represent intermontane basin ergs that formed a low elevation Paleogene desert [23,24]. The paleoelevation of this arid environment recorded by clumped and oxygen isotopes of the Relu Basin was only 0.6 km during ~50–45 Ma. According to previous studies, a similar arid environment prevailed across interior southern China [25,26,58], dominated by a sub-tropical high-pressure system [27,28]. However, the age of these widespread desert deposits has long been controversial, but in the Relu Basin the pyroclastic rocks on top of the aeolian dune deposits directly constrain their upper age limit to be 45 Ma.

After 45 Ma, aeolian sand dune deposition in the Relu Basin ceased and a fully lacustrine depositional environment capturing multiple layers of plant fossils had become established by 42 Ma. This not only represents a transition from a hot-dry to a relatively humid climate, but it may also suggest a monsoon climate may have begun to affect the Relu Basin at this time. Correspondingly, most of the Paleogene basins in eastern Tibet (e.g., the Jianchuan Basin to the southwest of the Relu Basin) also exhibit similar changes in sedimentary facies (from desert to lacustrine, arid to humid), which could be interpreted as regional-scale evidence of increased moisture supply for the eastern Tibet, but such simple increases in humidity do not necessarily mean the establishment of the modern Asian monsoon or any of its sub-systems. Furthermore, we note that in the Jianchuan Basin this arid-to-humid transition was recently constrained to ~41 [66] or ~36 Ma [28], which is younger than the 45–42 Ma age we have determined in the Relu Basin. The possible reason for this age discrepancy may be due to the complexity of the sedimentary sequence and poor outcrop conditions in the Jianchuan Basin, resulting in inappropriate judgments as to the location of the dating material within the succession. In particular, the age of ~36 Ma is based on the lamprophyre intruded into the overlying lacustrine and interbedded volcano-clastics, and as such only constrains the youngest possible age of the lacustrine units, not their actual age of deposition. In contrast, our age results were based on dating of volcanic tuffs within a continuous sedimentary section in the Relu Basin, which fixes precisely the time of the arid-to-humid transition.

Plant fossils in the Relu Basin provide more direct evidence for the initiation of a monsoon. Our CLAMP analyses of both the TR1 (45–42 Ma) and TR3 (42–40 Ma) assemblages in the lacustrine strata reveal monsoon-adapted traits. They also indicate an elevation rise from ~2 to ~3 km, and an ~4 °C (20 to 16 °C) reduction in MAAT. Notably, precipitation exhibited an obvious monsoonal pattern, with a ratio between the three wettest months and the three driest months (3WET:3DRY) of 7:1 for TR1 and 6:1 for TR3. Although CLAMP does not return information directly as to when in the year the 3 wettest months occurred, VPD and PE values suggest that winter was when most moisture was available to the Relu plants. This is not a feature of the SAM, but is seen most often in the EAM and the so-called transitional area (TA) that prevails over eastern Tibet and Yunnan today (Table S4 online). Both TR1 and TR3 show that VPD was highest (driest) in the summer, which can occur in the modern EAM but many modern EAM sites show the highest VPD values to be in either spring or autumn. In the modern SAM the highest VPD tends to be in the spring (Table S4 online), showing that the monsoon experienced by TR1 and TR3 cannot be easily characterized in terms of any of the modern Asian monsoon systems.

The existence of a monsoon is also recorded by fossil mammal teeth preserved in the Relu Formation. δ^{18}O values measured at equal intervals in intact mammalian teeth (samples 2020SL01 and 2020SL02; Fig. 3aa, bb) exhibit obvious oscillations (Fig. S13 online), which we attribute to seasonal variations in precipitation caused by a monsoonal climate, with δ^{18}O values showing enrichment in dry months and deficits in wet months [18]. We note that these pronounced monsoonal signals only appear after the Relu Basin had achieved elevations of 3.5 km in the late Eocene (~39–34 Ma), and we envisage this change was driven by the elevation of eastern Tibet as shown in our numerical simulation.

Both proxy evidence and climate simulations provide mutual support for the development of monsoonal conditions in eastern Tibet during the Eocene concurrent with local uplift. Under the scenario where high Gangdese and Central Watershed mountains bound a deep-wide valley with a low (open) eastern end, our model results show that the entire eastern Tibet region would have been arid (Fig. 6a1–e1), consistent with the observed desert-like climate. With the rise of eastern Tibet, a strong seasonally variable increase in precipitation developed and both eastern Tibet and eastern Asia became significantly wetter (Fig. 6a2–e2). The consistency in monsoonal signal derived from both model and proxy data point to the end of an arid climate and the spread of a monsoonal climate across eastern Tibet during the middle-late Eocene.

Congruent model and proxy data suggest that with the middle to late Eocene rise of eastern Tibet to its present-day elevation, the prior Inter-tropical Convergence Zone type monsoon system expanded significantly beyond the tropics and penetrated into subtropical eastern Tibet [18,24,28,67]. This is possibly because the high-altitude landform of the Gangdese extending to eastern Tibet both strengthened differential heating between land and ocean and deflected prevailing winds [1,2,4,67], so allowing tropical airmasses to penetrate further north. In middle-Eocene time, after 45 Ma, an orographically modified monsoonal climate was already beginning to impact the Relu Basin and eastern Tibet.

4.3. What kind of monsoon developed over eastern Tibet in the Eocene?

Documenting the evolution of the different modern Asian monsoon subsystems (SAM, EAM, and TA) is not straightforward because geological proxies that just return signals of seasonal variations in growth or environmental conditions (e.g., growth lines in shells, teeth, or wood, or varved sediments) cannot easily distinguish between temperature or precipitation variations, and in the case of precipitation do not identify when in the year the wet and dry seasons occurred. In Asia it is usually assumed that any seasonality signal implies a summer-wet regime as at present, but this need not be so. At mid latitudes (30°–60°) today several winter-wet climates (e.g., in the Mediterranean region, California and Chile) exist with clearly differentiated wet and dry seasons. For proxy paleorecords of seasonality in Asia it is not inevitable that they reflect the modern summer-wet regime, or that past monsoon systems were identical, or even similar, to those of the present [20].

The CLAMP results point to both VPD and PE being lower in the winter than the summer (Table S3 online), suggesting winters were when most moisture was available to plants. However, cooler winter temperatures alone could increase humidity. Our climate simulations show that with an open Central Tibetan Valley, winds would have penetrated from the west in the winter and in the middle of this valley, for example across the Lunpola Basin, a winter-wet regime with minimal summer rainfall predominated [68]. This external moisture supply was, however, limited so the fluvial and lacustrine facies preserved in the Lunpola Basin evidence water sources high in the catchment regions of the bounding mountains. Further east along the Central Valley the winter westerlies become drier, and what little rainfall did reach the area came from the south during the summer (Fig. 6d1), producing a summer-wet system, but quite unlike that of the modern SAM. As eastern Tibet rose, moist airflow from the south increased due to the strengthening of differential heating of land and ocean, but was also blocked by the rising landform. Adiabatic cooling as moist air parcels rose against this obstruction increased precipitation in eastern Tibet, some of which crested the landform and spilled westward into the Central Valley. This precipitation pattern, however, is clearly bimodal, with precipitation occurring mostly in spring and autumn (Fig. 6c2, e2), contributing, along with cooler temperatures, to higher winter humidity. Although different from the summer-wet monsoon we see today, the distinctly seasonal pattern of precipitation in the Eocene shows it is monsoonal. These results signify an orographically amplified Asian monsoon system, but one that is neither the modern SAM nor the EAM nor typical of the TA.

4.4. Eocene high biodiversity in the Hengduan mountains

The Hengduan Mountains, eastern Tibetan Plateau, are well known for their high species diversity, complex terrain and monsoonal climate, which make this region a global biodiversity hotspot [7,8]. It now seems that high biodiversity, similar to that of the present, was established sometime in the Eocene [7,29,30], but the roles of tectonics and climate in generating this diversity remain unclear, as are the spatial patterns of that change.

The TR1–TR3 Relu Basin plant fossil assemblages are dominated by angiosperm leaves, and the most abundant forms belong to "*Eucalyptus*" (Fig. 3a, o). We put quotes around "*Eucalyptus*" because it's true biological affinity is uncertain, but the name is useful in that it conveys its overall appearance. The form "*Myrtophyllum*" is just as appropriate [40]. This leaf type exists within assemblages with high species richness representing subtropical, evergreen, broad-leaved forests, and shows that high plant diversity existed in the Hengduan Mountains by the middle Eocene (45–40 Ma), albeit with a composition that is quite unusual compared to that existing in eastern Tibet today. Apart from "*Eucalyptus*", most taxa can still be assigned to modern genera, with some such as *Palibinia*, *Ulmus*, *Comptonia*, *Lonicera*, *Viburnum* and *Albizzia* being widely distributed in Paleogene strata in China, but others (e.g., Menispermaceae, Myrtaceae, *Banksia*, *Myrica*, *Comptonia* and *Trapa*) even occurring in Paleogene strata in North America [69,70]. In addition, the Relu floral assemblage is also closely related to Eocene central Asia floras in that taxa such as *Chamaecyparis*, *Arundo*, *Palibinia*, *Myrica* and *Rhus* are shared with the Eocene Er-Oilan-Du3 fossil assemblage in Turkmenistan [40,71]. They all exhibit foliar features that are indicative of a warm environment, and suggest a relatively free exchange of plant lineages across the Northern Hemisphere during the Eocene greenhouse world. They also highlight the importance of the eastern Tibet flora to the migration and evolution of Asian species as a whole.

A previous study of the Markam Basin flora [12], west of the Relu Basin, shows that modern plant diversity in the Hengduan Mountains appeared no later than the late Eocene, and that a modernization "speciation pump" was deeply rooted in the Paleogene [7]. This is also evidenced by other highly diverse species found in the southern part of the Hengduan Mountains, such as in the Shuanghe flora [31], the Lühe flora [29,32], and the Wenshan flora [30], which is one of the most taxon-rich fossil floras in China. These assemblages point to diversification and modernization of the flora in Southwest China, including in the Hengduan Mountains, being underway in the late Eocene. The well-dated Relu flora now shows this diversification was already progressing in the middle Eocene. Note that these fossil finds all subvert previous molecular phylogenetic studies that suggested modern biodiversity was a product of the Miocene [72].

This diversity is also reflected by the fauna. Abundant vertebrates, especially mammalian fossils of at least 8 families and 12 genera (*Anthracokeryx Litangensis, Caenolophus proficiens, Bothriodon* sp., *Sianodon* sp., *Yuomys* sp., Brontotheriidae indet., Rhinocerotidae indet., Anthracotheriidae indet., Leporidae indet., and Testudinidae indet., etc.) occur in the upper Relu Formation (~39–34 Ma). This shows that eastern Tibet hosted a highly diverse fauna in the late Eocene, including both herbivores and carnivores, with the most abundant being Perissodactyla. Moreover, the Lijiang Basin of Yunnan, just south of the Relu Basin, hosts the middle-late Eocene Xiangshan fauna that is also highly diverse [73], preserving 9 families and 17 genera of mammals, including *Lijiangia zhangi*, *Anthracothema lijiangensis*, *Teleolophus xiangshanensis*, *Anthracokeryx sinensis*, *Eomoropus minimus*, *Prohyracodon major*, *Diplolophodon similis*, *Rhodopagus yunnanensis*, *Grangeria canina*, and *Diplolophodon similis*, amongst others. Overall, the regional diversity and duration of both flora and fauna implies that the present biodiversity in the Hengduan Mountains began to take shape in the middle Eocene and this emphasizes both the value and antiquity of Asia’s exceptional biota.

The development of a monsoonal climate synchronous with the rise of eastern Tibet likely promoted the globally significant regional biotic assembly. The Eocene monsoon system, although it differed from its present-day form, was characterised by seasonal precipitation and annual temperature variations and, combined with newly-formed pronounced relief and a warm climate background, produced high levels of fluctuating environmental niche complexity [74,75], thus stimulating high speciation rates and, ultimately, the Hengduan Mountain global biodiversity hotspot that enhanced biodiversity modernisation across eastern Asia.

5. Conclusions and implications

The rise of eastern Tibet, the development of a monsoonal climate across eastern Asia and the evolution of exceptionally high regional biodiversity were synchronous. Early in the Eocene (~50–45 Ma), eastern Tibet was a low-elevation hot-dry desert with few plants and animals. During the middle Eocene (45–40 Ma), eastern Tibet rose and, in response, an Eocene monsoon expanded northwards initiating the development a diverse Asian evergreen broadleaved forest. By the late Eocene (~39–34 Ma), with the establishment of near-modern topography in eastern Tibet, a highly diverse biota emerged (Fig. S14 online) as the monsoon developed further, laying the foundations of the modern exceptionally diverse regional biota. However, the form of this Asian monsoon was quite different from those of today, in that it featured bimodal precipitation with particularly humid winters, and so does not mark the establishment of any of the modern Asian monsoons.

This Eocene-specific monsoon points to modern Asian monsoon systems being a product of subsequent orographic evolution within the Tibetan region (e.g., the rise of the Himalaya) combined with global environmental changes such as global cooling, changes in paleogeography and ocean circulation (e.g., the opening of the Drake Passage). There was no point in the past when modern Asian monsoons suddenly appeared. The modern monsoons are unique to the present and a product of a long gradual development in the context of an ever-changing Earth system.

Conflict of interest

The authors declare that they have no conflict of interest.

Acknowledgments

This work was supported by the National Natural Science Foundation of China project Basic Science Centre for Tibetan Plateau Earth System (41988101), the Second Tibetan Plateau Scientific

Expedition and Research Program (2019QZKK0708), the Strategic Priority Research Program of the Chinese Academy of Sciences (XDA20070301), the National Natural Science Foundation of China-Natural Environment Research Council of the United Kingdom Joint Research Program (41661134049 and NE/P013805/1), and the National Natural Science Foundation of China (41941016). We appreciate Lin Li from the University of Arizona and two anonymous reviewers for their detailed and constructive comments which greatly improved the quality of the manuscript. The thanks also go to Ciren Lamu and Feipeng Li from the State Key Laboratory of Tibetan Plateau Earth System, Environment and Resources, Institute of Tibetan Plateau Research, Chinese Academy of Sciences for their assistance and hard work in the field.

Author contributions

Lin Ding designed research; Songlin He, Zhongyu Xiong, Robert A. Spicer, Alex Farnsworth, Paul J. Valdes, Cao Wang, Fulong Cai, Houqi Wang, Yong Sun, Deng Zeng, Jing Xie, Yahui Yue, Chenyuan Zhao, Peiping Song, and Chen Wu performed research; Songlin He, Yahui Yue, and Chao Wang contributed to the zircon U-Pb measurements and XRD anlysis; Robert A. Spicer and Songlin He performed the CLAMP analysis; Alex Farnsworth, Paul J. Valdes, and Robert A. Spicer worked on the model simulations; Songlin He and Jing Xie contributed to the clumped and stable isotope analyses, as well as the experiments of grain size; and Songlin He, Lin Ding, Robert A. Spicer, Zhongyu Xiong, and Alex Farnsworth wrote the manuscript.

Appendix A. Supplementary materials

Supplementary materials to this article can be found online at

References

[1] Molnar P, Boos WR, Battisti DS. Orographic controls on climate and paleoclimate of Asia: thermal and mechanical roles for the Tibetan Plateau. Annu Rev Earth Planet Sci 2010;38:77–102.

[2] Farnsworth A, Lunt DJ, Robinson SA, et al. Past East Asian monsoon evolution controlled by paleogeography, not CO_2. Sci Adv 2019;5:eaax1697.

[3] Wu G, Liu Y, He B, et al. Thermal controls on the Asian summer monsoon. Sci Rep 2012;2:404.

[4] Thomson JR, Holden PB, Anand P, et al. Tectonic and climatic drivers of Asian monsoon evolution. Nat Commun 2021;12:4022.

[5] Boos WR, Kuang Z. Dominant control of the South Asian monsoon by orographic insulation versus plateau heating. Nature 2010;463:218–22.

[6] Chen F, Ding L, Piao S, et al. The Tibetan Plateau as the engine for Asian environmental change: the Tibetan Plateau Earth system research into a new era. Sci Bull 2021;66:1263–6.

[7] Spicer RA, Farnsworth A, Su T. Cenozoic topography, monsoons and biodiversity conservation within the Tibetan Region: an evolving story. Plant Divers 2020;42:229–54.

[8] Ding W-N, Ree RH, Spicer RA, et al. Ancient orogenic and monsoon-driven assembly of the world’s richest temperate alpine flora. Science 2020;369:578–81.

[9] Deng T, Wang X, Wu F, et al. Review: implications of vertebrate fossils for paleo-elevations of the Tibetan Plateau. Glob Planet Change 2019;174:58–69.

[10] Li S-F, Valdes PJ, Farnsworth A, et al. Orographic evolution of northern Tibet shaped vegetation and plant diversity in eastern Asia. Sci Adv 2021;7:eabc7741.

[11] Xie G, Sun B, Li J-F, et al. Fossil evidence reveals uplift of the central Tibetan Plateau and differentiated ecosystems during the Late Oligocene. Sci Bull 2021;66:1164–7.

[12] Su T, Spicer RA, Li S-H, et al. Uplift, climate and biotic changes at the Eocene–Oligocene transition in south-eastern Tibet. Natl Sci Rev 2019;6:495–504.

[13] Wang B, Ho L. Rainy season of the Asian-Pacific summer monsoon. J Clim 2002;15:386–98.

[14] Acosta RP, Huber M. Competing topographic mechanisms for the summer Indo-Asian monsoon. Geophys Res Lett 2020;47:e2019GL085112.

[15] Tardif D, Fluteau F, Donnadieu Y, et al. The origin of Asian monsoons: a modelling perspective. Clim Past 2020;16:847–65.

[16] Sarr A-C, Donnadieu Y, Bolton CT, et al. Neogene South Asian monsoon rainfall and wind histories diverged due to topographic effects. Nat Geosci 2022;15:314–9.

[17] Ding L, Spicer R, Yang J, et al. Quantifying the rise of the Himalaya orogen and implications for the South Asian monsoon. Geology 2017;45:215–8.

[18] Licht A, van Cappelle M, Abels HA, et al. Asian monsoons in a late Eocene greenhouse world. Nature 2014;513:501–6.

[19] Huber M, Goldner A. Eocene monsoons. J Asian Earth Sci 2012;44:3–23.

[20] Spicer RA, Yang J, Herman AB, et al. Asian Eocene monsoons as revealed by leaf architectural signatures. Earth Planet Sci Lett 2016;449:61–8.

[21] Bhatia H, Khan MA, Srivastava G, et al. Late Cretaceous–Paleogene Indian monsoon climate vis-à-vis movement of the Indian plate, and the birth of the South Asian monsoon. Gondwana Res 2021;93:89–100.

[22] Shukla A, Mehrotra RC, Spicer RA, et al. Cool equatorial terrestrial temperatures and the South Asian monsoon in the Early Eocene: evidence from the Gurha Mine, Rajasthan, India. Palaeogeogr Palaeoclimatol

Palaeoecol 2014;412:187–98.

[23] Jiang X, Cui X, Wu H, et al. The Palaeogene deserts and their implications for the origin of monsoons on the eastern margin of the Qinghai-Xizang Plateau, SW China. Sediment Geol Teth Geol 2012;32:54–63 (in Chinese).

[24] Xiong Z, Ding L, Spicer RA, et al. The early Eocene rise of the Gonjo Basin, SE Tibet: from low desert to high forest. Earth Planet Sci Lett 2020;543:116312.

[25] Sun X, Wang P. How old is the Asian monsoon system?—Palaeobotanical records from China. Palaeogeogr Palaeoclimatol Palaeoecol 2005;222:181–222.

[26] Liu X, Guo Q, Guo Z, et al. Where were the monsoon regions and arid zones in Asia prior to the Tibetan Plateau uplift? Natl Sci Rev 2015;2:403–16.

[27] Zhang Z, Flatøy F, Wang H, et al. Early Eocene Asian climate dominated by desert and steppe with limited monsoons. J Asian Earth Sci 2012;44:24–35.

[28] Zheng H, Yang Q, Cao S, et al. From desert to monsoon: irreversible climatic transition at similar to 36 Ma in southeastern Tibetan Plateau. Prog Earth Planet Sci 2022;9:12.

[29] Linnemann U, Su T, Kunzmann L, et al. New U-Pb dates show a Paleogene origin for the modern Asian biodiversity hot spots. Geology 2018;46:3–6.

[30] Tian Y, Spicer RA, Huang J, et al. New early oligocene zircon U-Pb dates for the ‘Miocene’ Wenshan Basin, Yunnan, China: biodiversity and paleoenvironment. Earth Planet Sci Lett 2021;565:116929.

[31] Huang Y, Jia L, Wang Q, et al. Cenozoic plant diversity of Yunnan: a review. Plant Divers 2016;38:271–82.

[32] Wu M, Huang J, Spicer RA, et al. The early Oligocene establishment of modern topography and plant diversity on the southeastern margin of the Tibetan Plateau. Glob Planet Change 2022;214:103856.

[33] Jackson WT, Robinson DM, Weislogel AL, et al. Mesozoic development of Nonmarine Basins in the northern Yidun Terrane: deposition and deformation in the eastern Tibetan Plateau prior to the India-Asia collision. Tectonics 2018;37:2466–85.

[34] Todrani A, Zhang B, Speranza F, et al. Paleomagnetism of the Middle Cenozoic Mula Basin (East Tibet): evidence for km-scale crustal blocks rotated by midlower crust drag. Geochem Geophys Geosyst 2020;21:e2020GC009225.

[35] Fick SE, Hijmans RJ. WorldClim 2: new 1-km spatial resolution climate surfaces for global land areas. Int J Climatol 2017;37:4302–15.

[36] Quade J, Rech JA, Latorre C, et al. Soils at the hyperarid margin: the isotopic composition of soil carbonate from the Atacama Desert, Northern Chile. Geochim Cosmochim Acta 2007;71:3772–95.

[37] Kelson JR, Huntington KW, Schauer AJ, et al. Toward a universal carbonate clumped isotope calibration: diverse synthesis and preparatory methods suggest a single temperature relationship. Geochim Cosmochim Acta 2017;197:104–31.

[38] Dickinson WR, Gehrels GE. Use of U-Pb ages of detrital zircons to infer maximum depositional ages of strata: a test against a Colorado Plateau Mesozoic database. Earth Planet Sci Lett 2009;288:115–25.

[39] Gong H, Li Q, Ni X. New species of *Yuomys* (Rodentia, Ctenodactyloidea) from the upper Eocene of eastern Ningxia, China. J Vertebr Paleontol 2021;41:e1938099.

[40] Guo S. An Eocene flora from the Relu Formation in Litang county of Sichuan and the history of Eucalyptus. In: Sun H, editor. Studies in Qinghai-Xizang (Tibet) Plateau special issue of Hengduan mountains scientific expedition II. Beijng: Beijing Publishing House of Science and Technology; 1986. p. 66–70 (in Chinese).

[41] Eiler JM. "Clumped-isotope" geochemistry—The study of naturally-occurring, multiply-substituted isotopologues. Earth Planet Sci Lett 2007;262:309–27.

[42] Ghosh P, Adkins J, Affek H, et al. ^{13}C–^{18}O bonds in carbonate minerals: a new kind of paleothermometer.

Geochim Cosmochim Acta 2006;70:1439–56.

[43] Hoke GD, Liu-Zeng J, Hren MT, et al. Stable isotopes reveal high southeast Tibetan Plateau margin since the Paleogene. Earth Planet Sci Lett 2014;394:270–8.

[44] Quade J, Eiler J, Daëron M, et al. The clumped isotope geothermometer in soil and paleosol carbonate. Geochim Cosmochim Acta 2013;105:92–107.

[45] Rowley DB, Garzione CN. Stable isotope-based paleoaltimetry. Annu Rev Earth Planet Sci 2007;35:463–508.

[46] Kim S-T, O'Neil JR. Equilibrium and nonequilibrium oxygen isotope effects in synthetic carbonates. Geochim Cosmochim Acta 1997;61:3461–75.

[47] Westerhold T, Marwan N, Drury AJ, et al. An astronomically dated record of Earth's climate and its predictability over the last 66 million years. Science 2020;369:1383–7.

[48] Zachos JC, Stott LD, Lohmann KC. Evolution of early Cenozoic marine temperatures. Paleoceanography 1994;9:353–87.

[49] Zhang W, Fang X, Zhang T, et al. Eocene rotation of the northeastern central Tibetan Plateau indicating stepwise compressions and eastward extrusions. Geophys Res Lett 2020;47:e2020GL088989.

[50] Chen W, Zhang S, Ding J, et al. Combined paleomagnetic and geochronological study on Cretaceous strata of the Qiangtang terrane, central Tibet. Gondwana Res 2017;41:373–89.

[51] Tong Y, Yang Z, Mao C, et al. Paleomagnetism of Eocene red-beds in the eastern part of the Qiangtang terrane and its implications for uplift and southward crustal extrusion in the southeastern edge of the Tibetan Plateau. Earth Planet Sci Lett 2017;475:1–14.

[52] Bowen GJ, Wilkinson B. Spatial distribution of δ^{18}O in meteoric precipitation. Geology 2002;30:315–8.

[53] Spicer RA, Yang J, Spicer TEV, et al. Woody dicot leaf traits as a palaeoclimate proxy: 100 years of development and application. Palaeogeogr Palaeoclimatol Palaeoecol 2021;562:110138.

[54] Forest CE, Molnar P, Emanuel KA. Palaeoaltimetry from energy conservation principles. Nature 1995;374:347–50.

[55] Su T, Spicer RA, Wu FX, et al. A Middle Eocene lowland humid subtropical "Shangri-La" ecosystem in central Tibet. Proc Natl Acad Sci USA 2020;117:32989–95.

[56] Li L, Fan M, Davila N, et al. Carbonate stable and clumped isotopic evidence for late Eocene moderate to high elevation of the east-central Tibetan Plateau and its geodynamic implications. Geol Soc Am Bull 2018;131:831–44.

[57] Xu Q, Liu X, Ding L. Miocene high-elevation landscape of the eastern Tibetan Plateau. Geochem Geophys Geosyst 2016;17:4254–67.

[58] Guo Z, Sun B, Zhang Z, et al. A major reorganization of Asian climate by the early Miocene. Clim Past 2008;4:153–74.

[59] Liu-Zeng J, Zhang J, McPhillips D, et al. Multiple episodes of fast exhumation since Cretaceous in Southeast Tibet, revealed by low-temperature thermochronology. Earth Planet Sci Lett 2018;490:62–76.

[60] Liu F, Danišík M, Zheng D, et al. Distinguishing tectonic versus climatic forcing on landscape evolution: an example from SE Tibetan Plateau. Geol Soc Am Bull 2020;133:233–42.

[61] Cao K, Tian Y, van der Beek P, et al. Southwestward growth of plateau surfaces in eastern Tibet. Earth Sci Rev 2022;232:104160.

[62] Kapp P, Yin A, Harrison TM, et al. Cretaceous-Tertiary shortening, basin development, and volcanism in central Tibet. Geol Soc Am Bull 2005;117:865–78.

[63] Ding L, Kapp P, Yue Y, et al. Postcollisional calc-alkaline lavas and xenoliths from the southern Qiangtang terrane, central Tibet. Earth Planet Sci Lett 2007;254:28–38.

[64] Ding L, Kapp P, Cai F, et al. Timing and mechanisms of Tibetan Plateau uplift. Nat Rev Earth Environ

2022;doi: 10.1038/s43017-022-00318-4.
[65] Feng J, Yao H, Chen L, et al. Massive lithospheric delamination in southeastern Tibet facilitating continental extrusion. Natl Sci Rev 2022;9:nwab174.
[66] Fang X, Yan M, Zhang W, et al. Paleogeography control of Indian monsoon intensification and expansion at 41 Ma. Sci Bull 2021;66:2320–8.
[67] Bosboom RE, Abels HA, Hoorn C, et al. Aridification in continental Asia after the Middle Eocene Climatic Optimum (MECO). Earth Planet Sci Lett 2014;389:34–42.
[68] Xiong Z, Liu X, Ding L, et al. The rise and demise of the Paleogene Central Tibetan Valley. Sci Adv 2022;8:eabj0944.
[69] Chen M, Kong Z, Chen Y. On the discover of palaeogene flora from the western Sichuan Plateau and its significance in phytogeography. Acta Bot Sin 1983;25:482–93 (in Chinese).
[70] Jacques FMB, Guo S-X. Palaeoskapha sichuanensis gen. et sp nov (Menispermaceae) from the Eocene Relu Formation in western Sichuan, West China. Acta Phytotaxon Sin 2007;45:576–82.
[71] Vasilevskaya ND. Eocene flora of Badkhyz in Turkmenistan. In: The collection in memory of Krishtofovich AN. Moscow-Leningrad: Soviet Academy of Sciences; 1957. p. 103–75 (in Russian).
[72] Lu L-M, Mao L-F, Yang T, et al. Evolutionary history of the angiosperm flora of China. Nature 2018;554:234–8.
[73] Zong G, Chen W, Huang X, et al. Cenezoic mammals and environment of Hengduan Mountains region. Beijing: China Ocean Press; 1996 (in Chinese).
[74] Spicer RA. Tibet, the Himalaya, Asian monsoons and biodiversity—In what ways are they related? Plant Divers 2017;39:233–44.
[75] Antonelli A, Kissling WD, Flantua SGA, et al. Geological and climatic influences on mountain biodiversity. Nat Geosci 2018;11:718–27.

Songlin He is currently a Ph.D. candidate at the State Key Laboratory of Tibetan Plateau Earth System, Environment and Resources, Institute of Tibetan Plateau Research, Chinese Academy of Sciences. He received his B.S. degree (2017) in geology at the Chengdu University of Technology. His current research focuses on the quantitative reconstruction of paleoelevation and paleoclimate in the Cenozoic history of the Tibetan Plateau.

Lin Ding is an academician of Chinese Academy of Sciences, a full professor at the State Key Laboratory of Tibetan Plateau Earth System, Environment and Resources, Institute of Tibetan Plateau Research, Chinese Academy of Sciences, and an honorary fellow of the Geological Society of America. His expertise lies in continental tectonics, structural geology, geochemistry, and geochronology. His research interest focuses on the processes of oceanic convergence and continental collision, uplift of the Tibetan Plateau, and uplift-related effects on Asian climate.

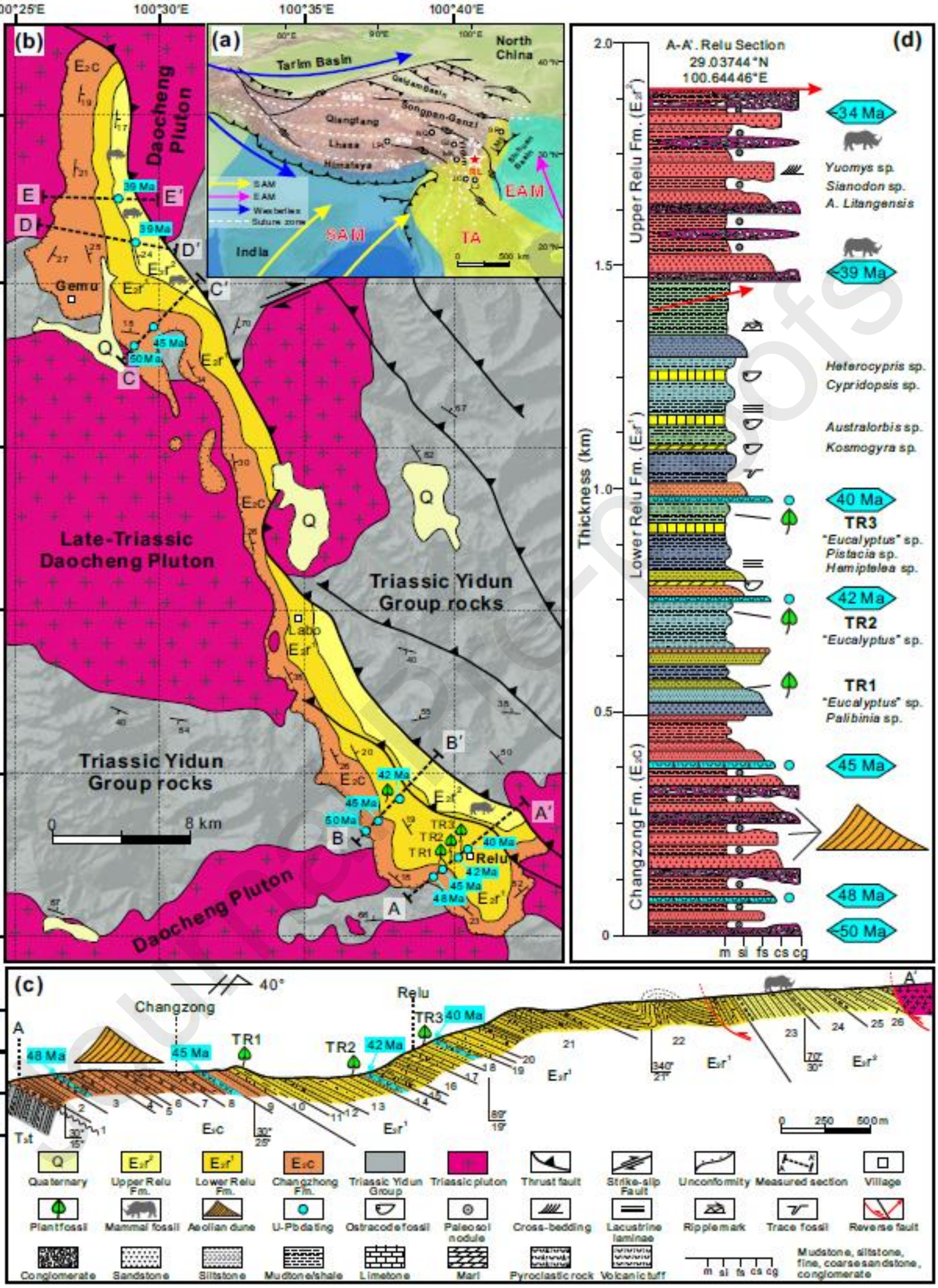
100°25'E
100°30'E
100°35'E
100°40'E
29°25'N
29°20'N
29°15'N
29°10'N
29°05'N
29°00'N
(b)
E2c
Daocheng Pluton
E
E'
D
D'
39 Ma
Gemu
E2r1
E2r2
C'
Q
C
45 Ma
50 Ma
Late-Triassic Daocheng Pluton
Triassic Yidun Group rocks
Labo
B'
B
A'
A
42 Ma
40 Ma
48 Ma
TR1
TR2
TR3
Relu
0
8 km
(a)
80°E
90°E
100°E
North China
40°N
30°N
20°N
Tarim Basin
Qaidam Basin
Songpan-Ganzi
Qiangtang
Lhasa
Himalaya
India
SAM
EAM
TA
RL
Sichuan Basin
Westerlies
Suture zone
0
500 km
(d)
A-A'. Relu Section
29.03744°N
100.64446°E
Upper Relu Fm. (E2r2)
Lower Relu Fm. (E2r1)
Changzong Fm. (E2c)
Thickness (km)
2.0
1.5
1.0
0.5
0
~34 Ma
Yuomys sp.
Sianodon sp.
A. Litangensis
~39 Ma
Heterocypris sp.
Cypridopsis sp.
Australorbis sp.
Kosmogyra sp.
40 Ma
TR3
"Eucalyptus" sp.
Pistacia sp.
Hemiptelea sp.
42 Ma
TR2
"Eucalyptus" sp.
TR1
"Eucalyptus" sp.
Palibinia sp.
45 Ma
48 Ma
~50 Ma
m si fs cs cg
(c)
40°
Changzong
Relu
Elevation (km)
3.9
3.7
3.5
3.3
T3t
E2c
E2r1
E2r2
340°
21°
70°
30°
30°
25°
89°
19°
30°
15°
0
250
500m
Quaternary
Upper Relu Fm.
Lower Relu Fm.
Changzhong Fm.
Triassic Yidun Group
Triassic pluton
Thrust fault
Strike-slip Fault
Unconformity
Measured section
Village
Plant fossil
Mammal fossil
Aeolian dune
U-Pb dating
Ostracode fossil
Paleosol nodule
Cross-bedding
Lacustrine laminae
Ripple mark
Trace fossil
Reverse fault
Conglomerate
Sandstone
Siltstone
Mudstone/shale
Limestone
Marl
Pyroclastic rock
Volcanic tuff
m si fs cs cg
Mudstone, siltstone, fine, coarse sandstone, conglomerate

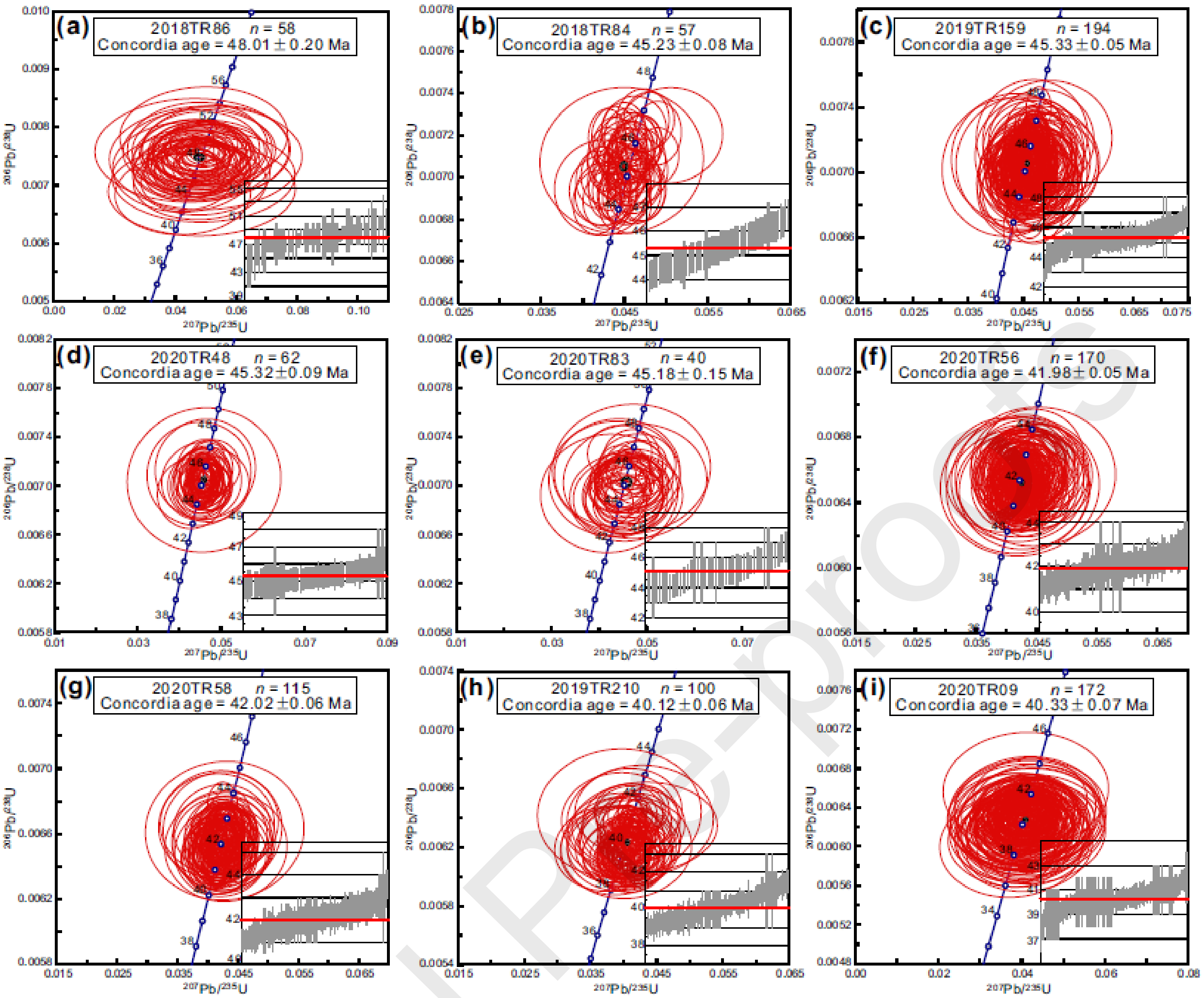
(a)
2018TR86 n = 58
Concordia age = 48.01 ± 0.20 Ma
(b)
2018TR84 n = 57
Concordia age = 45.23 ± 0.08 Ma
(c)
2019TR159 n = 194
Concordia age = 45.33 ± 0.05 Ma
(d)
2020TR48 n = 62
Concordia age = 45.32 ± 0.09 Ma
(e)
2020TR83 n = 40
Concordia age = 45.18 ± 0.15 Ma
(f)
2020TR56 n = 170
Concordia age = 41.98 ± 0.05 Ma
(g)
2020TR58 n = 115
Concordia age = 42.02 ± 0.06 Ma
(h)
2019TR210 n = 100
Concordia age = 40.12 ± 0.06 Ma
(i)
2020TR09 n = 172
Concordia age = 40.33 ± 0.07 Ma
²⁰⁶Pb/²³⁸U
²⁰⁷Pb/²³⁵U

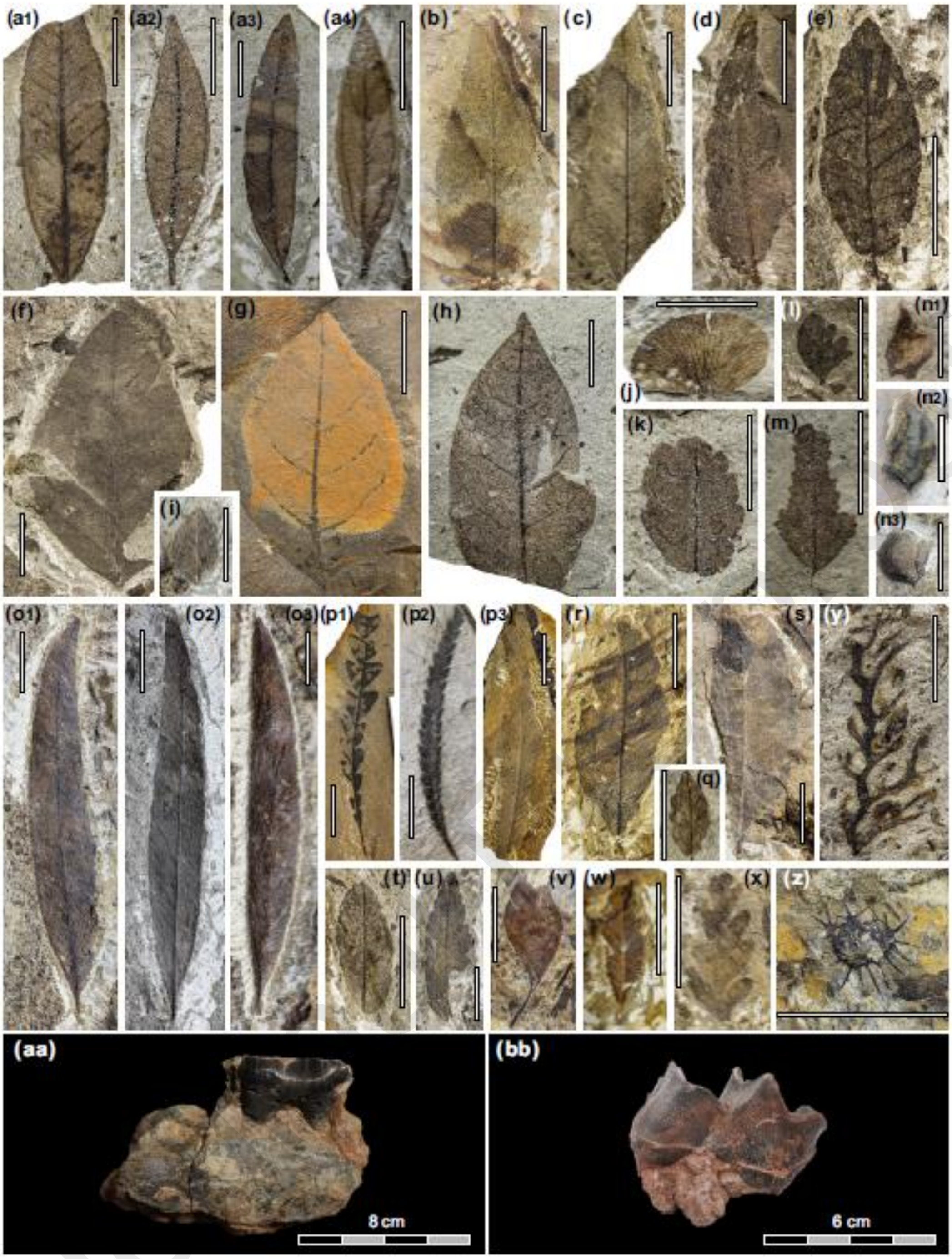
(a1)
(a2)
(a3)
(a4)
(b)
(c)
(d)
(e)
(f)
(g)
(h)
(i)
(j)
(l)
(n1)
(n2)
(n3)
(k)
(m)
(o1)
(o2)
(o3)
(p1)
(p2)
(p3)
(r)
(q)
(s)
(y)
(t)
(u)
(v)
(w)
(x)
(z)
(aa)
8 cm
(bb)
6 cm

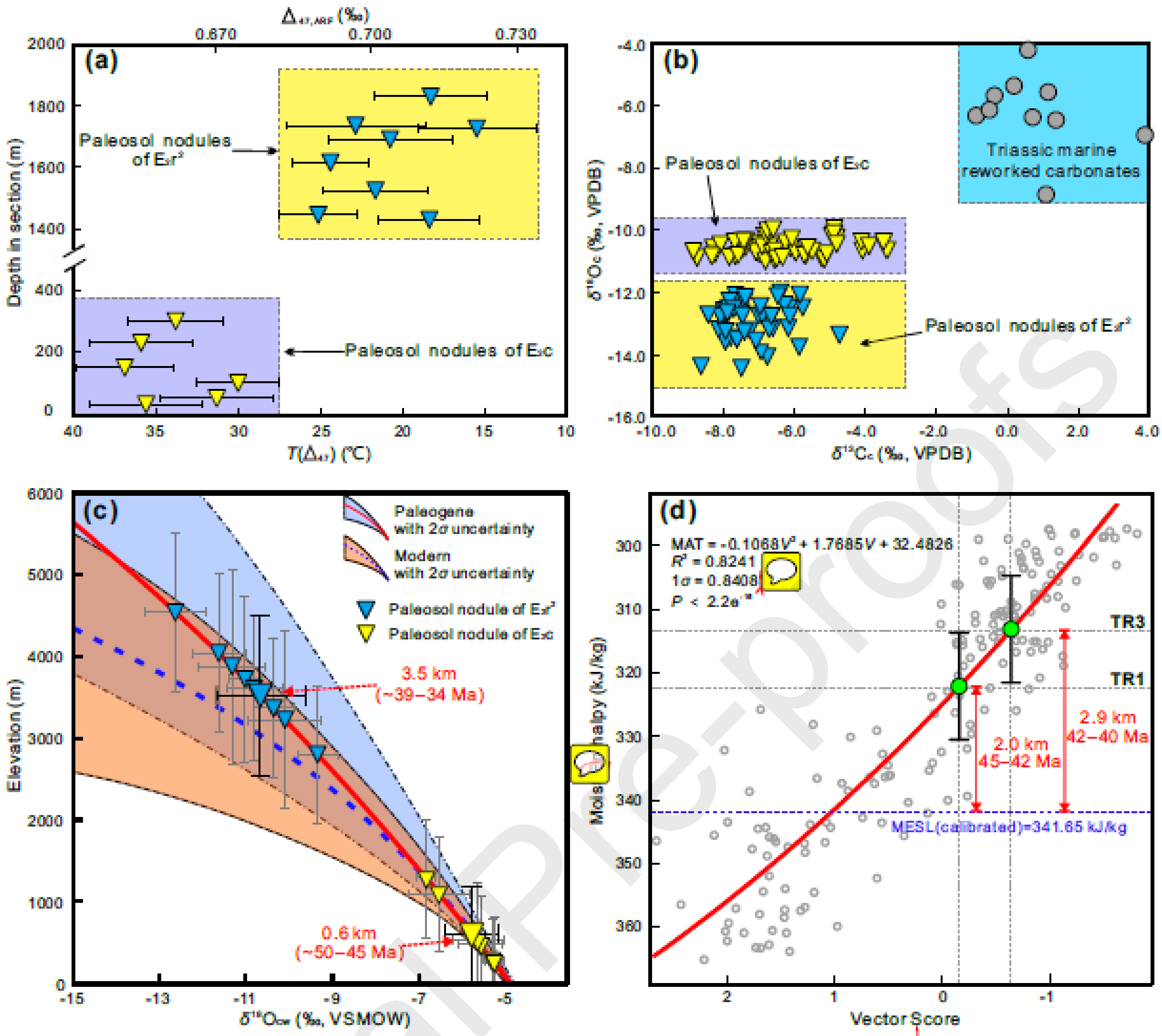
(a)
Δ47,ARF (‰)
0.670
0.700
0.730
Depth in section (m)
2000
1800
1600
1400
400
200
0
Paleosol nodules of E3r²
Paleosol nodules of E3c
40
35
30
25
20
15
10
T(Δ47) (°C)
(b)
-4.0
-6.0
-8.0
-10.0
-12.0
-14.0
-16.0
δ18Oc (‰, VPDB)
Paleosol nodules of E3c
Triassic marine reworked carbonates
Paleosol nodules of E3r²
-10.0
-8.0
-6.0
-4.0
-2.0
0.0
2.0
4.0
δ13Cc (‰, VPDB)
(c)
6000
5000
4000
3000
2000
1000
0
Elevation (m)
Paleogene with 2σ uncertainty
Modern with 2σ uncertainty
Paleosol nodule of E3r²
Paleosol nodule of E3c
3.5 km (~39–34 Ma)
0.6 km (~50–45 Ma)
-15
-13
-11
-9
-7
-5
δ18Ocw (‰, VSMOW)
(d)
MAT = -0.1068V² + 1.7685V + 32.4826
R² = 0.8241
1σ = 0.8408
P < 2.2e-16
300
310
320
330
340
350
360
Moist enthalpy (kJ/kg)
TR3
TR1
2.9 km 42–40 Ma
2.0 km 45–42 Ma
MESL(calibrated)=341.65 kJ/kg
2
1
0
-1
Vector Score

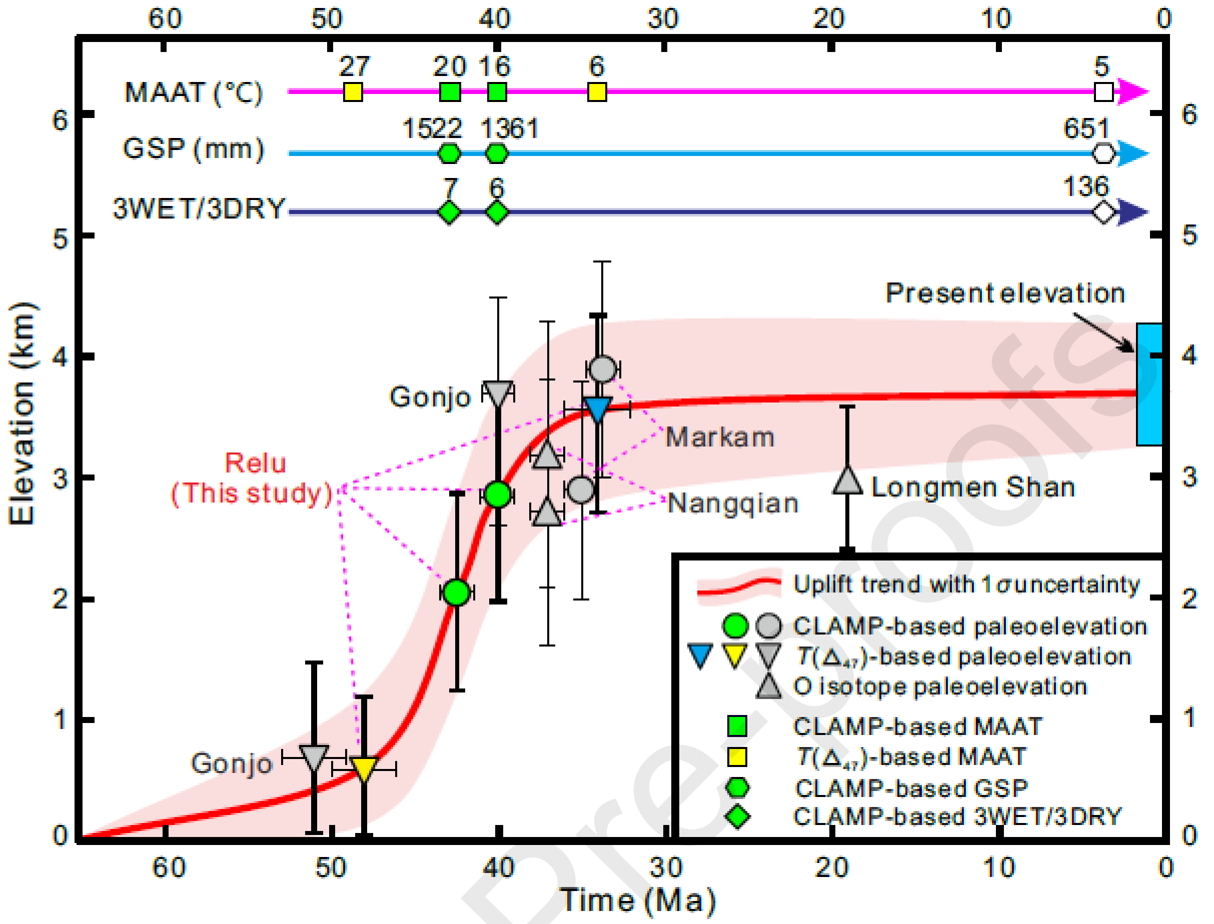
MAAT (°C)
27
20
16
6
5
GSP (mm)
1522
1361
651
3WET/3DRY
7
6
136
Present elevation
Gonjo
Relu
(This study)
Markam
Nangqian
Longmen Shan
Gonjo
Uplift trend with 1 σ uncertainty
CLAMP-based paleoelevation
$T(\Delta_{47})$-based paleoelevation
O isotope paleoelevation
CLAMP-based MAAT
$T(\Delta_{47})$-based MAAT
CLAMP-based GSP
CLAMP-based 3WET/3DRY
Elevation (km)
Time (Ma)
0
1
2
3
4
5
6
60
50
40
30
20
10
0

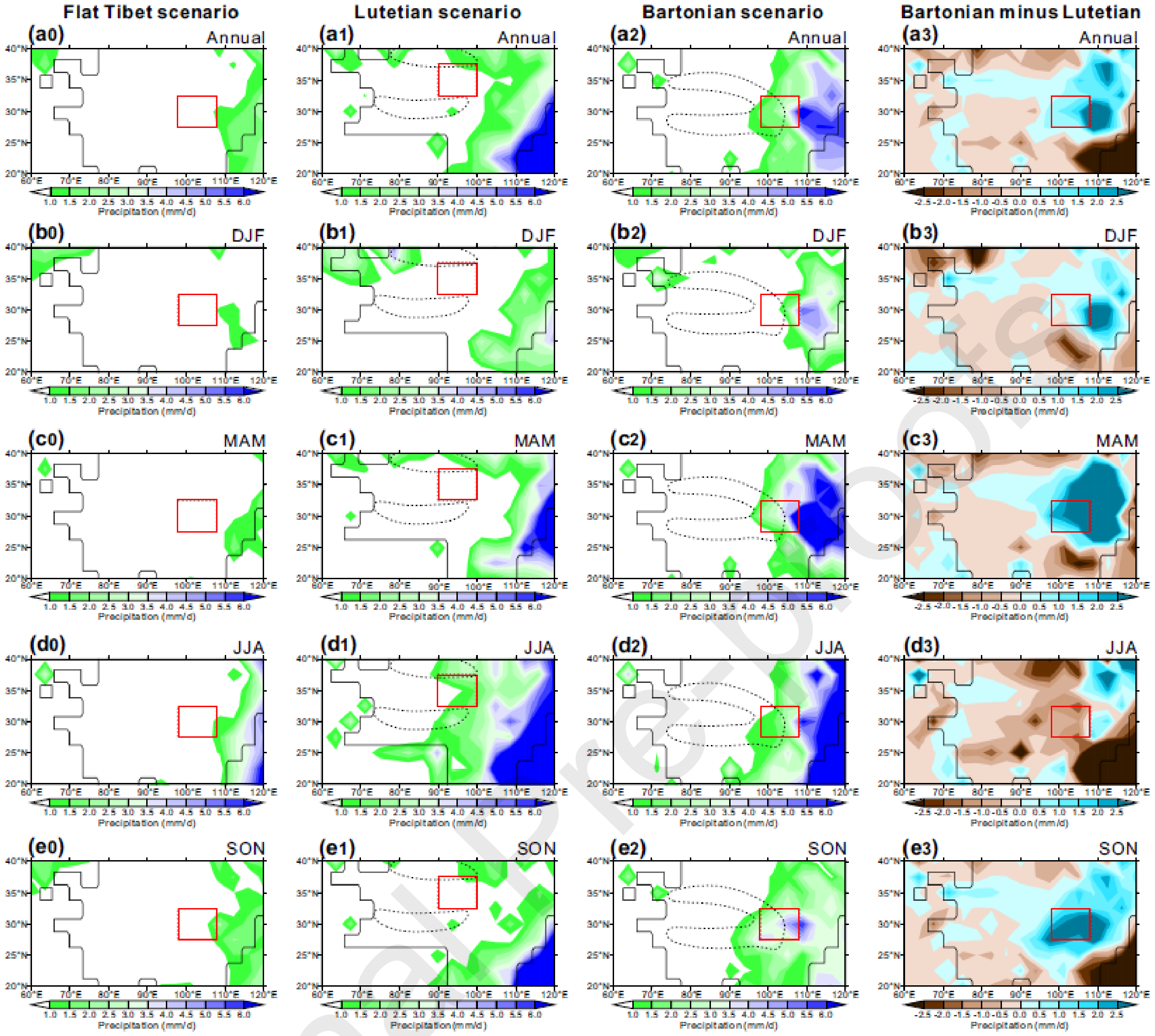
Flat Tibet scenario
Lutetian scenario
Bartonian scenario
Bartonian minus Lutetian
(a0) Annual
(a1) Annual
(a2) Annual
(a3) Annual
(b0) DJF
(b1) DJF
(b2) DJF
(b3) DJF
(c0) MAM
(c1) MAM
(c2) MAM
(c3) MAM
(d0) JJA
(d1) JJA
(d2) JJA
(d3) JJA
(e0) SON
(e1) SON
(e2) SON
(e3) SON
40°N
35°N
30°N
25°N
20°N
60°E
70°E
80°E
90°E
100°E
110°E
120°E
1.0 1.5 2.0 2.5 3.0 3.5 4.0 4.5 5.0 5.5 6.0
-2.5 -2.0 -1.5 -1.0 -0.5 0.0 0.5 1.0 1.5 2.0 2.5
Precipitation (mm/d)

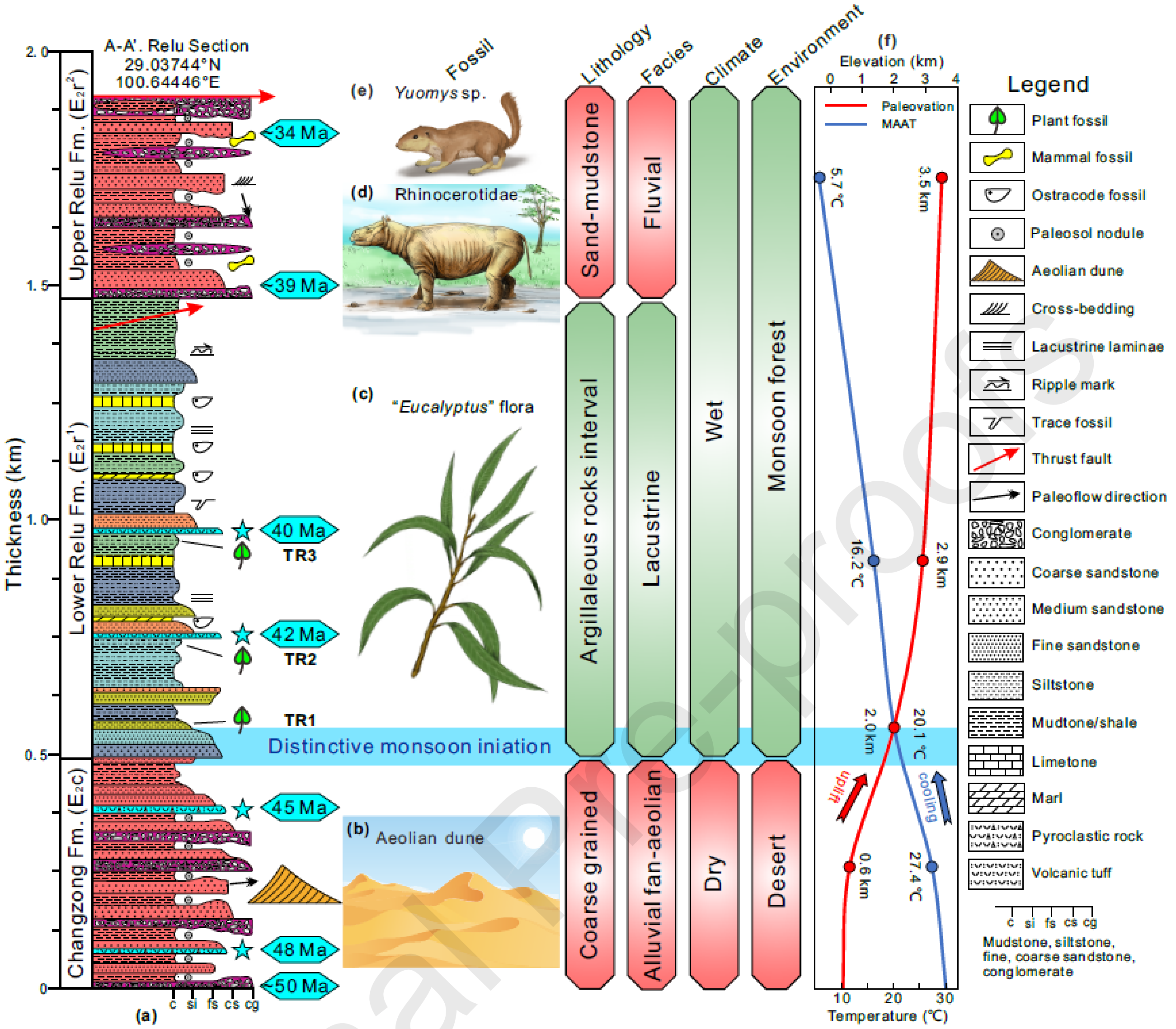
A-A'. Relu Section
29.03744°N
100.64446°E
Thickness (km)
2. 0
1. 5
1. 0
0. 5
0
Upper Relu Fm. (E_2r^2)
Lower Relu Fm. (E_2r^1)
Changzong Fm. (E_2c)
34 Ma
39 Ma
40 Ma
TR3
42 Ma
TR2
TR1
45 Ma
48 Ma
50 Ma
c si fs cs cg
(a)
Fossil
(e) Yuomys sp.
(d) Rhinocerotidae
(c) "Eucalyptus" flora
(b) Aeolian dune
Distinctive monsoon iniation
Lithology
Facies
Climate
Environment
Sand-mudstone
Fluvial
Argillaleous rocks interval
Lacustrine
Wet
Monsoon forest
Coarse grained
Alluvial fan-aeolian
Dry
Desert
(f)
Elevation (km)
0 1 2 3 4
Paleovation
MAAT
5.7 °C
3.5 km
16.2 °C
2.9 km
2.0 km
20.1 °C
uplift
cooling
0.6 km
27.4 °C
10 20 30
Temperature (°C)
Legend
Plant fossil
Mammal fossil
Ostracode fossil
Paleosol nodule
Aeolian dune
Cross-bedding
Lacustrine laminae
Ripple mark
Trace fossil
Thrust fault
Paleoflow direction
Conglomerate
Coarse sandstone
Medium sandstone
Fine sandstone
Siltstone
Mudtone/shale
Limetone
Marl
Pyroclastic rock
Volcanic tuff
c si fs cs cg
Mudstone, siltstone, fine, coarse sandstone, conglomerate